

Use of a 4D Planispheric Transformation for the Tracking and the Analysis of LV Motion with Tagged MR Images

Jérôme Declerck, Nicholas Ayache, Elliot R. Mcveigh

▶ **To cite this version:**

Jérôme Declerck, Nicholas Ayache, Elliot R. Mcveigh. Use of a 4D Planispheric Transformation for the Tracking and the Analysis of LV Motion with Tagged MR Images. RR-3535, INRIA. 1998. inria-00073150

HAL Id: inria-00073150
https://inria.hal.science/inria-00073150

Submitted on 24 May 2006

HAL is a multi-disciplinary open access archive for the deposit and dissemination of scientific research documents, whether they are published or not. The documents may come from teaching and research institutions in France or abroad, or from public or private research centers.

L'archive ouverte pluridisciplinaire **HAL**, est destinée au dépôt et à la diffusion de documents scientifiques de niveau recherche, publiés ou non, émanant des établissements d'enseignement et de recherche français ou étrangers, des laboratoires publics ou privés.



INSTITUT NATIONAL DE RECHERCHE EN INFORMATIQUE ET EN AUTOMATIQUE

Use of a 4D planispheric transformation for the tracking and the analysis of LV motion with tagged MR images

Jérôme Declerck, Nicholas Ayache, Elliot R. McVeigh

N° 3535

Octobre 1998

THÈME 3



ISSN 0249-6399



Use of a 4D planispheric transformation for the tracking and the analysis of LV motion with tagged MR images

Jérôme Declerck*, Nicholas Ayache, Elliot R. McVeigh

Thème 3 — Interaction homme-machine,
images, données, connaissances
Projet Epidaure †

Rapport de recherche n° 3535 — Octobre 1998 — 37 pages

Abstract:

A major issue in cardiac imaging is the assessment of cardiac function and particularly the identification of ischemic or infarcted tissues. We present in this article a method to reconstruct the displacement field of the left ventricular (LV) motion using 4D planispheric transformations of time and space combined in a first step with B-spline tensor products.

Because of the 4D modeling, a) it is possible to include any tag plane direction as input data. b) The use of planispheric coordinates makes the numerical evaluation more stable as compared to prolate spheroidal coordinates, the equivalent focal point being much further from the apical area of the heart. This therefore avoids mathematical instability when the material points of the myocardium are too close to the apical focus. c) In the temporal modeling, a simple adaptation is possible to changing temporal dynamics, such as introduced by ectopic pacing or rapid filling after systole. d) Finally, the strain analysis and displacement parameters that are used for the spatial modeling are computed at any point of the LV volume.

Experiments are conducted on a normal and a pathological LV (posterior infarct) in order to assess the tuning of the parameters of the method. The mean RMS-distance error is less than 0.5mm for both LVs. Finally, the motion is analysed as zeroth (displacement) and first order parameters (strain), which estimate are smooth.

Key-words: non-rigid matching, 4D, medical image, cardiology, tagged MRI.

* E-mail: jdecler@mri.jhu.edu
† http://www.inria.fr/Equipes/EPIDAURE-eng.html

Unité de recherche INRIA Sophia Antipolis
2004, route des Lucioles, B.P. 93, 06902 Sophia Antipolis Cedex (France)

Suivi et analyse du mouvement à partir d'images IRM marquées avec des transformations planisphériques 4D

Résumé : Un des enjeux majeurs de l'imagerie cardiologique est l'évaluation de la fonction ventriculaire, particulièrement la détection des tissus ischémiques ou infarcis. Nous présentons dans ce rapport une méthode pour reconstruire le mouvement du ventricule gauche à partir d'images IRM marquée (tagged MRI) grâce à des transformations planisphériques 4D de l'espace et du temps, combinées avec des produits tensoriels de B-splines.

Grâce à la modélisation en 4D, a) il est possible d'inclure des directions de marquage quelconques. b) L'utilisation de coordonnées planisphériques rend le calcul numérique plus stable qu'en utilisant des coordonnées "prolate spheroid", le point focal correspondant étant suffisamment éloigné de l'apex pour rester loin du myocarde. Cela évite des problèmes d'instabilité numérique quand ce foyer est proche de l'apex. c) La paramétrisation temporelle est modifiable de manière à respecter la dynamique temporelle telle qu'elle peut apparaître lors de l'étape rapide de remplissage en début de systole, ou bien lors d'une stimulation de contraction. d) Enfin, l'analyse des déplacements est calculée en tout point du volume du ventricule gauche et est continue en temps et en espace.

Des expériences ont été réalisées sur un cœur normal et un cœur pathologique (infarctus postérieur), de manière à assurer le réglage des paramètres de la méthode. L'erreur constaté dans la reconstruction est inférieure à 0.5mm en moyenne dans les deux cas.

Mots-clés : mise en correspondance non-rigide, 4D, image médicale, cardiologie, IRM.

Introduction

A major issue in cardiac imaging is the assessment of cardiac function and particularly the identification of ischemic or infarcted tissues [12]. Modern techniques provide 3D images which describe either the anatomy of the heart (MRI, for instance) or its functionality (Nuclear Medicine PET or SPECT imaging, for instance). It is possible to get sequences of such images over the whole cardiac cycle; such sequences are real 3D movies of the motion of the heart. The cardiac motion, like the motion of any real object in the body must be therefore described as a 4D continuous and regular transformation of time and space.

We consider here the problem of tracking and analysing the motion of the LV from tagged MR images [3, 23]. The whole space is tagged with a set of planes that deform with the tissue, providing non-invasive markers that feature the local displacement of the myocardium. The intersection of those tagging planes with the imaging plane appear as dark lines in the images.

Many methods have been proposed to use this information. First, it is necessary to identify the tag lines. Different techniques are reported in the litterature using pattern matching [9], snakes [13, 21] or spline modeling [1, 17, 16], with a different level of automation, none being fully automatic at this time. As the tag lines are only intersections of the image plane and the deformed tag plane, the reconstruction of the motion is an ill-posed problem using only one series of images. Using the strategy of [19, 10], which consists in acquiring three different series of images of the same heart using orthogonal tagging directions, the motion can be reconstructed, using either constrained models [20, 19, 22] or free-form deformations [7, 21, 18, 10] as in this article.

Unfortunately, because the correspondence is defined between two successive images, regularity and periodicity in time are not guaranteed. We define a 4D planispheric transformation (4DPT, [6]) as a function of time and space deforming a point $\overrightarrow{\mathbf{x}}$ into a point $\overrightarrow{\mathbf{x}'}$ which is supposed to be the location of point $\overrightarrow{\mathbf{x}}$ at time t:

$$\begin{array}{rcl} f : \mathbb{R}^3 \times \mathbb{R} & \longrightarrow & \mathbb{R}^3 \\ (\overrightarrow{\mathbf{x}}, t) & \longmapsto & \overrightarrow{\mathbf{x}'} = f(\overrightarrow{\mathbf{x}}, t) \end{array}$$

This definition of the 4D transformation yields the definition of 2 categories of functions which are easier to understand and which are intrinsically regular:

$$\begin{array}{rcll} Traj_{\overrightarrow{\mathbf{x}}} & = & f(\overrightarrow{\mathbf{x}}, \cdot) & \text{is the trajectory of } M \text{ over time,} \\ D_t & = & f(\cdot, t) & \text{is the deformation function of the object at time } t. \end{array}$$

The 4DPT combines several properies which suit well to problem of tracking the LV motion from tagged MR:

1. it defines a class of transformation of **time** and **space** in which the **temporal continuity and potential periodicity** are included,

2. it defines a class of **highly constrained** transformations in order to have a **relevant** description of the LV motion with a **reduced** number of parameters,

3. it is able to retrieve canonical motions with minimal computation, providing an easy-to-interpret **quantitative analysis** of the motion,
4. the equations are written in such a way that there is **no mathematical singularity** at the apex due to the use of a polar system,
5. last, but not least, it is a transformation which combines the unknown parameters **in a linear way** to make their estimation easier and robust.

The paper is organised as follows: in section 1, we explain the method we use to retrieve the motion information from tag data. In section 2, we recall the definition on the 4DPT and explain how to estimate it from the data. Experiments on human heart data are presented in section 3, these experiments are discussed in section 4, before drawing a conclusion on this work.

1 Tag displacement field reconstruction

1.1 The problem

We introduce here a few notations that are illustrated on figure 1. Let us consider the tag surfaces S_n at time t_n. At tagging time t_T, those surfaces S_T are planes with known normal n_T. The surface S_n intersects the slice at a line L_n.

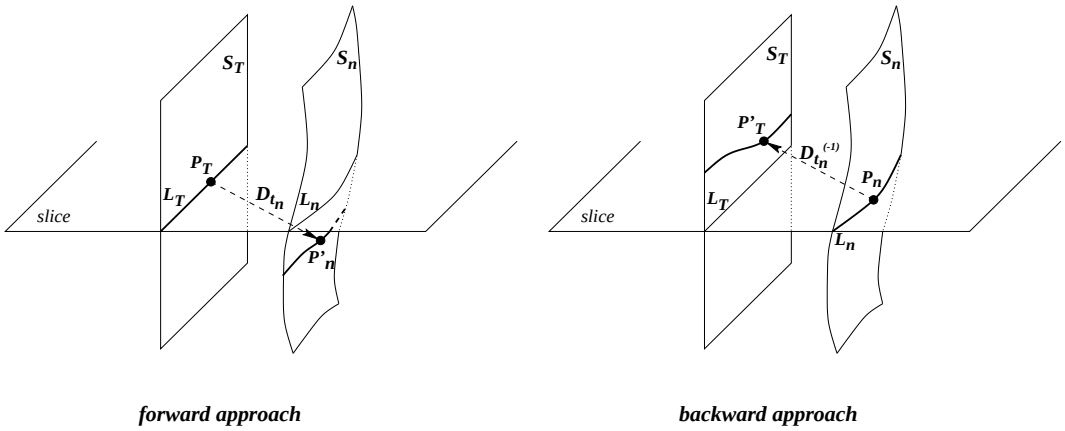


Figure 1: The tag plane at tagging time S_T deforms into surface S_n at time t_n. Left, the forward approach estimates the mapping which deforms S_T onto S_n and right, the backward approach estimates the mapping which deforms S_n back onto S_T.

1.1.1 Forward approach

The forward approach consists in estimating the deformations D_{t_n} given points P_T on different tag lines L_T and target points P_n at time t_n (figure 1, left). In order to write explicitely

the constraint $(D_{t_n}(P_T) \in S_n)$, we need to know the equation of the surface of S_n, and therefore it is necessary to model its shape.

In [15], this surface is interpolated with thin plate splines [4]. The authors compute the intersection of any 3 orthogonal planar surfaces it is possible to define in the surface, these intersection points featuring the same material point in the sequence. The displacement field is therefore estimated only at discrete locations. In [18], the tag surfaces (deformed tag planes at each time frame, traced as lines in each slices) are interpolated with B-spline surfaces. Intersecting the tag surfaces in a similar way as it is done in [15], the deformation is computed from those landmark points with a finite element method using polynomial element basis (p-version of the finite element). In [21], the deformation model for the deformation D_{t_n} is a B-spline tensor product (called by the authors "B-solid"). The tag detection is combined with the estimation of the deformation, which is processed as a minimization of the energy of a 3D-snake. This energy integrates the work of internal forces for regularity constraints and external forces that push the B-solid into the tag lines. This latter method has been only applied for a stack of short-axis slices with SPAMM tag pattern without integrating any long axis displacement information.

1.1.2 Backward approach

Here, the methods estimate the deformation $\Phi_{n\to T}$ which defines the location at tagging time t_T of a point P_n taken at time t_n.

$$\Phi_{n\to T}(P_n) \quad = \quad P'_T \tag{1}$$

$\Phi_{n\to T}$ is thus the inverse of the 4D transformation at time t_n (figure 1, right):

$$\Phi_{n\to T} \quad = \quad [D_{t_n}]^{(-1)}$$

The vectorial equation (1) can be decomposed into 3 scalar equations which allow to estimate $\Phi_{n\to T}$ at P_n. From the planar tag deformation, it is only possible to write one of those three, the one that corresponds to the direction of the normal to the tag plane. As a matter of fact, the only thing we know about P_n is that at time t_T, it was in the plane S_T: its location within this plane is not determined (see figure 2):

$$\Phi_{n\to T}(P_n) \in S_T \tag{2}$$

As the equation of S_T is a plane, the constraint (2) is easier to write than in the case of the forward approach, where S_n can be a surface of complex shape which would have to be modeled. For a given point P, if the tag plane equation is noted:

$$\begin{aligned} a.x + b.y + c.z - d &= 0 \\ \Longleftrightarrow \qquad \boldsymbol{P}.\boldsymbol{n}_T &= d \end{aligned}$$

equation (2) can be rewritten :

$$\Phi_{n\to T}(P_n).\boldsymbol{n}_T \quad = \quad d \tag{3}$$

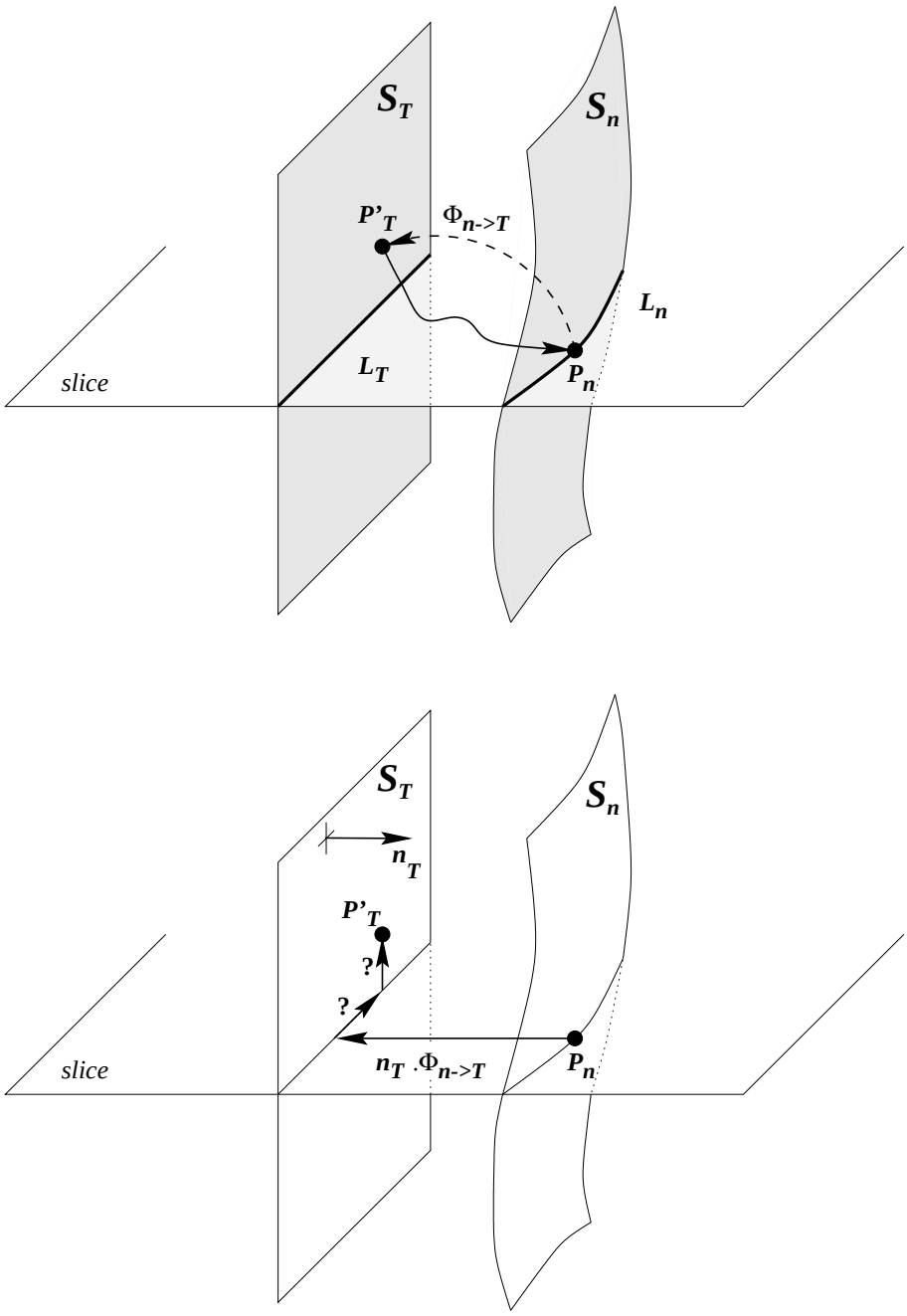


Figure 2: Top, a tag plane S_T is deformed at time t_n so that it becomes a surface S_n, which intersects the slice at a line L_n. A point P_n of this line was a point P'_T in S_T at tagging time t_T. Bottom, it is only possible to estimate the displacement $\boldsymbol{P_n P'_T}$ in the direction of the normal to the tag plane $\boldsymbol{n}_T$, but not in plane S_T.

Using at least three independent directions for $\boldsymbol{n}_T$, the problem is no longer underdetermined and the transformation $\Phi_{n\to T}$ can be estimated.

Some techniques have been implemented to reconstruct a dense displacement field from constraints (3) written for every tag point. In [22], the left ventricle is modelled with a finite element mesh whose basis functions are defined by heuristics. In [19], the model is a prolate spheroid deformed with spherical harmonics functions. Both of them are dedicated to the LV motion, due to the a priori in the geometry they use. In [10], the displacement field is reconstructed by formulating a stochastic estimation criterion from finite differences model.

For all those methods, the forward transformation is computed by point-to-point inversion with an arbitrary precision. In this article, we propose a method for which we compute the backward transformation with B-splines tensor products, the forward transformation is then a 4D planispheric transformation whose estimation is based on the B-splines backward transformations.

1.2 B-splines tensor product for the backward deformation

The aim is here to estimate at each time frame n the transformation $\Phi_{n\to T}$. In order to get rid of heavy notations, we will rename as Φ the transformation we want to estimate. We use B-splines transformations using constraints (3), the definition and estimation of such functions is detailed in the next paragraphs.

1.2.1 Definition of the B-spline transformations

B-splines are piecewise polynomials of degree K that are defined by a set of knots and recursive formulae [11]. Those defined knots are the junction points between two consecutive polynomials, therefore they set the degree of continuity of the function at that point. Those functions define a basis of the vector space of the piecewise polynomials with specific continuity constraints at the knots. A B-spline curve is a linear combination of the B-spline basis functions.

For a transformation Φ which deforms a point P onto a point $Q = \Phi(P)$, the coordinates of the deformed point is defined as a tensor product of B-spline curves [7, 8], as for the B-solid defined in [21]:

$$\begin{aligned}
\Phi^x(x,y,z) &= \sum_{i=0}^{n^x-1}\sum_{j=0}^{n^y-1}\sum_{k=0}^{n^z-1} A^x_{ijk}.B^x_i(x).B^y_j(y).B^z_k(z) \\
\Phi^y(x,y,z) &= \sum_{i=0}^{n^x-1}\sum_{j=0}^{n^y-1}\sum_{k=0}^{n^z-1} A^y_{ijk}.B^x_i(x).B^y_j(y).B^z_k(z) \\
\Phi^z(x,y,z) &= \sum_{i=0}^{n^x-1}\sum_{j=0}^{n^y-1}\sum_{k=0}^{n^z-1} A^z_{ijk}.B^x_i(x).B^y_j(y).B^z_k(z)
\end{aligned}$$

where we define, for the x coordinate for instance, A^x as the set of control points, B^x_i the i-th B-spline basis function of degree K and n_x the number of control points. Here, we choose

cubic B-splines ($K = 3$) defined by a regular set of knots, ensuring a C^2 continuity of the transformation.

1.2.2 Estimation

Given the set of knots (or the number of control points) and the degree of the polynomials that define the basis functions, a transformation is fully determined by a set of control points A. In order to estimate such a set from tagged data, we minimize a least squares criterion which is defined as a sum of two terms:

1. *deformed tag points belong their original plane*

   Let us note (Φ^x, Φ^y, Φ^z) the cartesian coordinates of function Φ. For each tag plane of index p, its equation is $a_p.x + b_p.y + c_p.z - d_p = 0$, with $a_p^2 + b_p^2 + c_p^2 = 1$. p labels the planes for all the directions the data provides. Thus, each tag point $P_{p,i}$ at time n belonging to tag plane $S_{n,p}$ has coordinates $P_{p,i} = (P_{p,i}^x, P_{p,i}^y, P_{p,i}^z)$. The term $\mathcal{E}_{planes}$ is the normalized sum of the residual distances of the deformed $P_{p,i}$ to their tag plane $S_{T,p}$:

   $$\mathcal{E}_{planes}(\Phi) = \frac{1}{N.D^2} \sum_{p=1}^{P} \sum_{i=1}^{N_p} \left(a_p.\Phi^x(P_{p,i}) + b_p.\Phi^y(P_{p,i}) + c_p.\Phi^z(P_{p,i}) - d_p\right)^2$$

   N_p being the number of tag points in plane S_p, N the total number of points ($N = \sum_{p=1}^{P} N_p$) and D a normalisation distance featuring a characteristic size of the data. For this, we compute the centroid of the tag points and the distance is defined as the standard deviation of the distances of the tag points to this centroid.

2. *the deformation is smooth*

   The smoothing term is the normalised integral of the norm of the second derivative of Φ, as for [7, 8].

   $$\mathcal{E}_{smooth}(\Phi) = \frac{1}{D^3} \int_{\mathbb{R}^3} \left[\Phi_{xx}^2 + \Phi_{yy}^2 + \Phi_{zz}^2 + 2\,\Phi_{xy}^2 + 2\,\Phi_{yz}^2 + 2\,\Phi_{xz}^2\right]$$

   Minimizing this part tends to reinforce the stiffness of the transformation.

The final criterion is the weighted sum of those two terms:

$$\mathcal{E}(\Phi) = \mathcal{E}_{planes}(\Phi) + \rho.\mathcal{E}_{smooth}(\Phi) \tag{4}$$

The criterion is quadratic in the control points A^x, A^y and A^z. We are therefore ensured of finding a unique global minimum provided the criterion is positive definite. In our implementation, the criterion is miminized with a conjugate gradient method on the normal equation derived from (4).

The constraints like (2) are partial constraints on each point, we need three orthogonal equations like (2) so that the position of the point is well determined. Close to the boundaries of the myocardium, there is only one or two constraints instead of three (underdetermined problem), creating a singularity in the matrix: the term of the criterion $\mathcal{E}_{planes}$ is not positive definite, we need to add the smoothing term $\mathcal{E}_{smooth}$ so that the global criterion is positive definite and the normal matrix is invertible. Practically, without that smoothing term, a tag point deformed back to its plane might be stretched far away if it is close to a boundary [5].

The transformations $\Phi_{n\to T}$ $(n = 0..T-1)$ are estimated sequentially, using $\Phi_{(n-1)\to T}$ as the initial transformation for the conjugate gradient (identity for $n = 0$). With all the backward transformations, we compute a 4D planispheric transformation.

2 The 4D planispheric transformation

2.1 Definition

We recall here the basic definitions presented in [6]. The 4D planispheric transformation (4DPT) is adapted to describe with a minimum of parameters a complex motion such as the LV motion. This model of the deformation of the LV is a crude approximation compared to complex biomechanical models [14] or highly descriptive kinematic models [2], but it has enough freedom to describe both normal and pathological motions.

Given a point $\overrightarrow{\mathbf{x}}$ (x, y, z) in cartesian coordinates and a time value t, the transformation gives a point $\overrightarrow{\mathbf{x'}}$ (x', y', z') which is assumed to be the location of point M at time t. The cardiac motion is supposed to be regular in space and periodic in time. The 4DPT is therefore defined as a **differentiable** function in spatial variables x, y and z and as a **differentiable** and **periodic** function in time variable t.

The 4DPT f is defined in order to describe locally some specific motions of points on the myocardium. We approximate the shape of the left ventricle as a stretched sphere in the long-axis direction. This is, of course, a very crude approximation as the shape of the heart is much more complex, however our goal is not a precise definition of the shape of the muscle, but a plausible discrimination of characteristic motions.

For that particular purpose, we separate the motion of a point of the heart into three canonical orthogonal motions (Fig. 3):

- motion 1: a **radial motion** which decribes the contraction or dilatation of the whole structure towards a "center",
- motion 2: an **apico-basal rotation** (polar twist) around the apico-basal axis which describes the twisting motion of the LV points,
- motion 3: a motion (tangential to surfaces of constant r) which describes the **elevation** of the LV points in the apico-basal direction (the shortening of apex-base distance during systole).

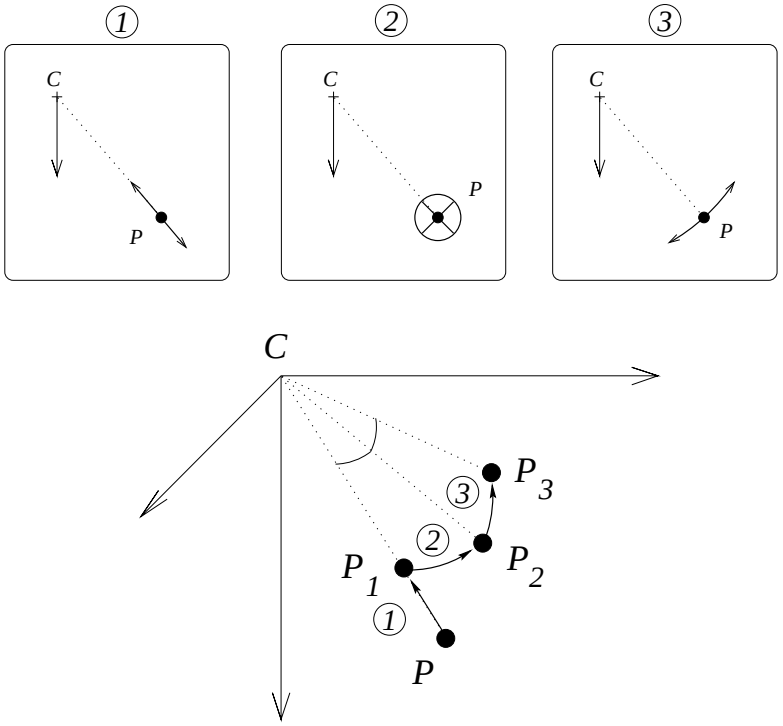


Figure 3: The top three frames illustrate the orthogonal motions described in the text. Bottom, point P is transformed in P_1 by the first motion (centripetal contraction), P_1 is transformed in P_2 by the second (apico-basal rotation) and P_2 is transformed in P_3 by the third one (elevation).

We describe these motions in a "3D-planispheric" coordinates system (PCS), which is a combination of spherical and cylindrical coordinates. Our tranformation function is thus defined as a composition of three functions:

$$f \quad = \quad P2C \circ f_P \circ C2P$$

The function $C2P$ switches from cartesian to 3D-planispheric coordinates, $P2C$ switches back from 3D-planispheric to cartesian coordinates (of course, $C2P = P2C^{-1}$). f_P is the function which is described with the three basic motions in 3D-planispheric coordinates. The next two paragraphs recall the definitions of these functions.

2.2 The planispheric coordinate system

In 3D cartesian space, we define a 3D-planispheric reference system given a center C, a base B and a set of two orthogonal vectors $\boldsymbol{u}$ (long axis direction from apex to base) and $\boldsymbol{v}$ (septum to lateral wall). For each point P, a center point H_P is defined on line (CB). From this center point, a distance $r = \|\boldsymbol{H_P P}\|$ and two angles (latitude θ and longitude φ) which are defined just as in the classical spherical coordinate system (figure 4). The position of H_P on the line CB is given by the following formula, for which a solution is described in [6]:

$$\boldsymbol{CH_P} \quad = \quad (1 - cos\theta)\, \boldsymbol{CB} \tag{5}$$

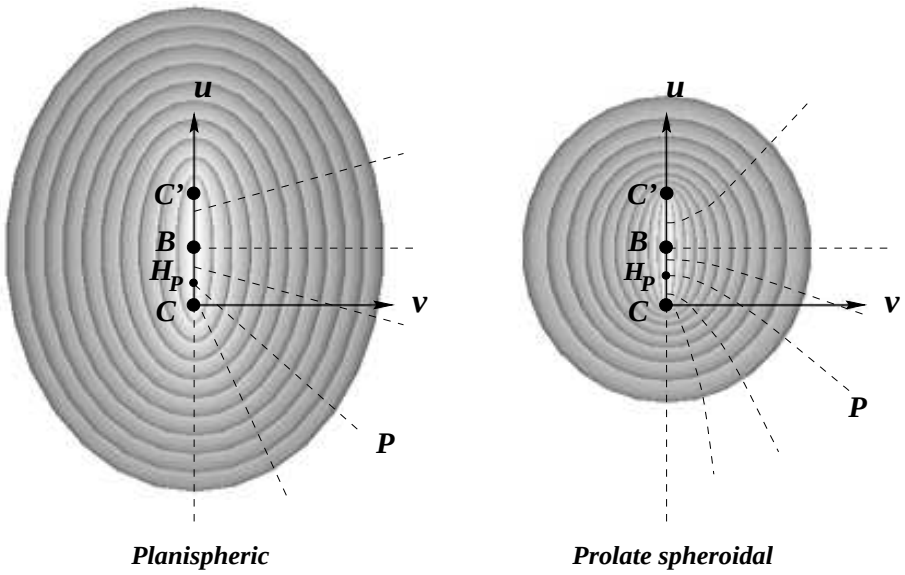


Figure 4: A representation of ten surfaces ($R = C^t$). The black lines show different points P and their associated center H_P for both planispheric and prolate spheroidal coordinate systems.

Finally, from the polar coordinates r, θ, φ, we compute the coordinates X, Y and R in this system as follows:

$$\begin{aligned} X &= \frac{\theta}{\pi}\cos(\varphi) \\ Y &= \frac{\theta}{\pi}\sin(\varphi) \\ R &= \frac{r}{\sigma_r} \end{aligned} \tag{6}$$

The two equations defining X and Y recalls the equations that define a projection of a map of the earth from one of its poles. This is why the word planispheric is used. The constant σ_r is a normalisation coefficient so that X, Y and R are dimensionless numbers of the same range.

The PCS is similar to the prolate spheroidal system, considering C and C' (its symmetric with respect to B) as the focal points and B as the center. There are some significant differences that make us prefer the PCS: the surfaces of constant θ are cones instead of single sheet hyperboloid surfaces. Moreover, the distance of surfaces of constant R (λ in prolate spheroidal) is closer in the apical area than around the basal circumference. Finally, and this is the most important difference, while fitting a set of real data to a surface of constant R, the optimal apical point in the prolate spheroidal system is closer to the apex than the one for PCS.

In our experiments, to fit an "optimal" coordinate system, we fit a surface of constant R to the epicardial contours that were defined by the user while segmenting the tag data. Using the prolate spheroidal system, the apical focus is so close to the apex that it may be included in the myocardium, creating some mathematical singularities spoiling the overall process of displacement field reconstruction as it may happen using [19], for instance (Fig. 5).

2.3 The 4D transformation in PCS

In the 3D-planispheric system, given a point P (X, Y, R), the transformed point P' (X', Y', R') through f_P is expressed as follows:

$$\begin{aligned} X' &= a_0 X - a_1 Y + a_2 \\ Y' &= a_1 X + a_0 Y + a_3 \\ R' &= a_4 R + a_5 \end{aligned} \tag{7}$$

The parameters a_p ($p = 0 \ldots 5$) are continuous and differentiable functions of r, θ, φ and t. In our formulation, we choose the parameters as polynomial functions in r and θ and quadratic B-splines in φ and t. Of course, the B-spline in φ is 2π-periodic, the B-spline in t may be periodic if desired, depending on the data. The transformation is explained in more detail in [6].

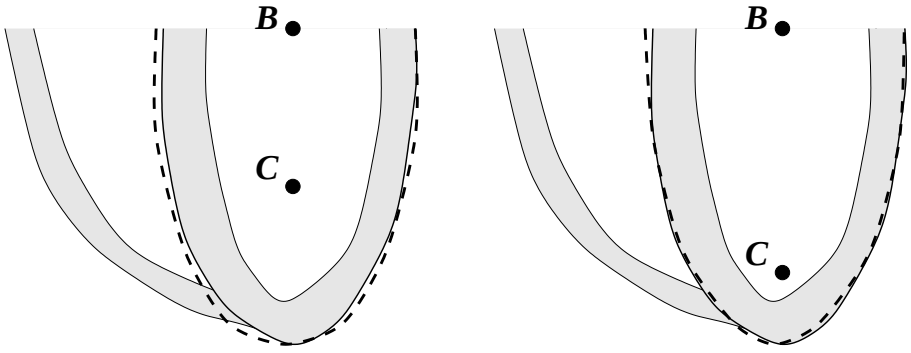


Figure 5: The LV epicardium (thick line) is fitted by a surface of constant R (dashed lines) in both planispheric (left) and prolate spheroidal (right) coordinate systems. Left, the apical focus (C) is in the middle of the cavity whereas on the right, it is close to the apex and may be included in the myocardial wall.

2.4 Motion parameters

These equations (7) can be described as a local 2D similarity in X and Y (a translation, a rotation and a uniform scaling) and a locally affine transformation in R. Using this description, we can write equations for the motion parameters we defined in section 2.1:

- radial motion: the a_4 factor,
- apico-basal rotation (polar twist): the angle of the 2D similarity,
- elevation: the scaling factor of the 2D similarity.

As those motions are computed directly from the displacement field, we call them "0th order parameter" as opposed to first order parameter like strain which is computed from the derivative (gradient) of the displacement field.

2.5 Estimation of the 4D transformation from tag data

In order to compute a 4DPT, we need to have a series of pairs of matched points between time t_T and each time frame t_n. For each n, each tag point $P_{n,m}$ is matched to its deformed tag point at t_T, which is estimated as being $\Phi_{n\to T}(P_{n,m})$. This point should be transformed by the TP4D f into $P_{n,m}$ itself. We thus can write a least squares criterion to estimate f as follows:

$$C(f) = \sum_n \sum_m \alpha_{n,m} \, . \, d\left(f\left(\Phi_{n\to T}(P_{n,m}), t_n\right) \; ; \; P_{n,m} \right)^2 \tag{8}$$

where $d(\cdot;\cdot)$ is the distance and $\alpha_{n,m}$ a weighting coefficient whose value is related to the reliability of the pair $[(\Phi_{n\to T}(P_{n,m}), t_n); P_{n,m}]$. Minimising C for f is done identically as in [6].

3 Experiments

The experiments of tag displacement field reconstruction with 4D planispheric transformations have been conducted on a normal patient and a pathological study. The pathological study is a LV of a patient who suffered from a 70 % LAD artery occlusion which induced an infarction in the posterior wall 8 days prior to imaging.

The images were acquired on a 1.5 T magnet (Signa 1.5T, GE Medical Systems, Milwaukee, WI) with a spoiled GRASS sequence (FOV = 32cm, TR = 3.6ms, TE = 1.5ms, flip angle = 12 deg) with partial k-space acquisition (11 lines of k-space per cardiac phase, tag plane normal parallel to the readout direction). The whole protocol necessitates around 20 heart beats (which is doable in one breathhold) for acquiring two slices. The sequence is composed of 11 time frames covering systole and early diastole (last two time slots). The time frames are equally spaced every 40 ms. We use 3 series of images, one of each is tagged in a direction: 2 sets of planar tags (SA0, SA90) perpendicular to the short axis plane and one (LA) orthogonal to the long axis planes. This samplig is the same as described in [19].

Figure 6 shows the region of interest selected in the image planes for the tag and contour extraction. It also shows some images of the normal heart at end diastole and at end systole. Figure 7 shows the tag and LV contour points segmented with the semi-automated package "FindTags" [13].

4 Results and Discussion

4.1 3D display of the LV motion

In order to control how the deformation fits with the tag data, the tag planes are computed and deformed at each time frame with the 4D transformation. Figure 8 shows the intersection of these deformed tag planes with the image slices, figure 9 shows these tags at three times of systole in wireframe display for all short axis slices. Long axis tags have been removed for clarity in this figure. The intersection points are computed so that they have the same abscissa along the tag line as do the original data points. We end up with a "simulated" set of tag points which has the same distribution as the original data set, which therefore allows us to compute the difference in position of the tag points as an offset in the direction of the normal to the tag plane. The tag lines are smoother than the original data and follow the tags in the images, as shown in figure 8.

With the 4D planispheric transformation, it is possible to apply the displacement field on the whole volume of the image. On figures 10 and 11, a mesh generated from the contour data is deformed over systole and displayed at three times (beginning, mid and end systole).

Thanks to the equations of the 4DPT, there is no mathematical singularity in the apical area, so the displacement of the apex can be visualised and controlled. In the infarcted case, it moves significantly more than for the normal case. As a matter of fact, the posterior wall, due to the infarction, does not contract in the same proportion than the anterior wall, and the apex is pulled towards the anterior wall. This is visually rendered in figure 12, in which the trajectories of some points of the mesh are displayed. Whereas there are 11 time slots, 20 points were used to interpolate the trajectory lines, which are, in our model, smooth quadratic B-spline curves.

4.2 Error analysis: choosing the number of control points

Figure 13 displays the rms-distance error graphs for the computed B-spline backward transformation at each time slot, for each series (SA0, SA90 and LA) and for all tag points. The distance which is computed is the distance of the tag point deformed by each $\Phi_{n\to T}$ to its original tag plane. The mean error are drawn for each time slot, a vertical segment of size the standard deviation of the distances shows the amplitude of the distribution around its mean. Time slot 8 corresponds to end systole, for which the deformation is greatest, inducing a peak in the error (around 0.3mm, with a standard deviation of 0.3mm). Figure 13 is generated with the transformation defined by 8x8x8 control points.

Figure 14 displays the rms-distance error graphs for the computed B-spline backward transformation at end systole for different number of control points, from 4x4x4 to 15x15x15. This display shows how to reasonably choose the number of control points so that the tensor product reliably models the deformation. The tag detection procedure has a theoretical accuracy of 0.1mm [13], assuming a perfect tag profile in the image and a tag CNR of at least 10. Practically, due to tag fading at late time slots, to the thickness of the slice (7mm) or to operator variability, it is more reasonable to assume that the tag detection precision is around 0.5mm at later time frames (pixel size being 1.25mm). Based on these considerations and other similar experiments [7], we fix the number of control points as 8x8x8; a good compromise between accurate deformation representation and noise insensitivity.

Figure 15 shows the error intrinsic to the process of inverting the backward transformations $\Phi_{n\to T}$ with the 4D transformation f. For all time frames, each tag point is deformed successively by $\Phi_{n\to T}$ and f. Theoretically, this is just an inversion step and the point should be back in its original position. The reported error is the residual distance between the deformed tag point and the original tag point. Vertical bars have a length of one standard deviation above and below the mean. Figure 16 show a similar display for points at end systole for different number of control points for the backward transformation, from 4 to 15, but keeping the number of control points of the 4D transformation to $n_r = 3$, $n_l = 4$, $n_p = 6$, $n_t = 6$. The mean error curve increases with the number of control points before reaching a plateau around a number of control point of 8. As a matter of fact, as the number of control points increase, the $\Phi_{n\to T}$ gets less and less smooth as it gains more degrees of freedom, the 4D transformation is less and less able to match the higher spatial frequencies the backward transformation is able to track. Therefore the 4D transformation cannot differentiate high

frequency deformation information from pure noise, which explains the plateau in the error map. These figures show how to choose the number of control points for the $\Phi_{n\to T}$ in correlation with the number of control points for f.

Figures 17 to 19 show statistics computed from the residual distance between simulated and real tag points, for different sets of control points for the 4D transformation (2x2x4x6, 3x4x6x6 and 4x4x8x6). The error decreases as the number of control points increases, 3x4x6x6 is a good trade-of between precision in the retrieval of the motion and computational cost. Figure 20 shows the evolution of the residual error with the number of control points for $\Phi_{n\to T}$. A similar behavior is noticed as in 16.

For our final choice of number of control points, the mean error and standard deviation is 0.45mm.

Figure 21 shows the residual distance between a tag point deformed by the backward transformation and its original plane for the pathological LV. Figure 22 shows the residual distance between simulated and original tag points for this pathological heart. Despite the motion is more complex than for the normal heart, the error remains at a mean value inferior to 0.5mm.

4.3 Motion parameter computation

4.3.1 Displacement parameters

The 4DPT definition provides a set of 0th order motion parameters (as opposed to first order parameters (like strain) which are derived from the gradient of the deformation): the centripetal contraction (radial displacement), the elevation and the polar twist (apico-basal rotation). Figures 23 to 28 show maps of the three parameters computed in the midwall. Each curve show the temporal evolution of the parameter at a particular location. The spatial evolution of the parameter goes from septal, anterior, lateral and posterior walls from left to right and from base to apex from top to bottom. Thanks to temporal modeling, each displayed curves is smooth.

1. radial displacement: the evolution of the radial motion is coherent in the normal case. the curve increases before bending down at end systole. The anterior wall show less displacement than the posterior wall, and the septal wall stays translated even in early diastole whereas the posterior wall moves back earlier to its end-diastolic location, as the curves bends down faster. In the pathological case, the infarcted posterior wall motion is low compared to the opposite normal wall (anterior). Only the anterior wall goes significantly closer to the center of the cavity, contributing to the reduction of its volume and therefore to the pumping efficiency.

2. elevation: this parameter shows the proportional shrinking in the direction of the long axis. Its value is globally lower for the pathological case, the lack of contractility of the posterior wall has a global influence on the motion of the LV wall. In the apical area, the wall is pulled and slides towards the anterior wall, inducing a high value of the parameter.

3. polar twist: this twist angle is the angle of the rotation in polar coordinates. The angle values do not correspond with cartesian space, they are similar to spherical angles in topography. The normal values of this parameters do not usually exceed 10 degrees, vary from positive values to negative from base to apex. In the pathological case, the motion is so complex and unbalanced than it induces a high local rotation of the wall.

A more precise analysis of the parameters needs a validation on a large database, which is not in the scope of this article. We want to demonstrate the quality of the displacement field reconstruction with planispheric transformations, and the ability to derive motion parameters. They describe local behavior of the displacement in three particular directions, but, as opposed to first order parameters, the distribution of their values can be different from a normal distribution in the entire LV even if the dysfunction remains localized in a particular wall. The strain analysis is more precise to detect the local dysfunctional area, but the 0th order parameters already show how this area can affect the global function of the heart.

4.3.2 Strain

From the displacement field, the strain is computed as in [19]. The Lagragian finite strain tensor E is computed from the gradient tensor F of the transformation f. E is related to F via the equation:

$$E = \frac{1}{2}[F^T F - I]$$

where I is the identity matrix. The diagonal elements of this tensor measure the stretching (if positive) or the compression (if negative) of the displacement in the corresponding direction. We compute here particularly the diagonal elements of the E tensor in the circumferential (c) and longitudinal (l) directions.

Figures 29 and 31 show the circumferential and longitudinal strains E_{cc} and E_{ll} in the midwall for the normal LV, the tensor is computed with the 4D transformation (thick lines) and with the "TEA" program [19] (thin lines). The "TEA" program computes the displacement field as spherical harmonics defined in a prolate spheroidal geometry for each time frame independently. There is no time smoothing or time continuity constraints. Therefore, the strain values have some local jumps between successive time frames that are highly unlikely.

On the normal LV, the strains E_{cc} and E_{ll} computed with both methods are highly similar, despite some local variations (in the apex, mainly, this is due to the close vicinity of the apical focus of the prolate coordinate system which is very close to the myocardium and spoils the displacement field fitting process).

On the infarcted LV, figures 30 and 32, the TEA method shows more local variations in space and local jumps in time. The E_{ll} strain is slightly underestimated in the lateral wall with TEA compared to the values computed with the 4D transformation.

A more extensive comparison between the TEA program and the 4DPT is currently under study and will be the subject of a forthcoming article. The aim is here to show how

close the relults are from the state of the art methods, highlighting points where there may be some significant improvement.

5 Conclusion

In this article, we present a new method for tracking the motion of the left ventricle from planar tagged MR images. The 4D planispheric transformation, used in gated SPECT motion tracking [6] is applied to the tagged MR modality. First, 3D B-spline tensor products are computed to reconstruct the backward displacement field and a 4DPT is estimated from the backward transformations and the tag points data. With these transformation, it is possible to compute the motion with a reduced number of parameters thanks to their compact definition. The motion is modeled as a 4D continuous displacement function in time and space, some zeroth (motion) and first order (strain) parameters are derived from the computed motion. Experiments have been conducted on a normal and a pathological heart (LV posterior infarct). The mean error of the tracking procedure is less than 0.5mm, and the strain computation is comparable to the related litterature with the advantage of describing its evolution as a continuous function of time and space.

6 Acknowledgements

We would like to thank Cengizhan Öztürk, MD, PhD, for his judicious comments on this project. This work is supported by the French National Institute for Research in Computer Science and Control (INRIA, B.P. 93, 06902 Sophia Antipolis, France) and NIH grant HL45683. Dr. McVeigh is an Established Investigator of teh American Heart Association.

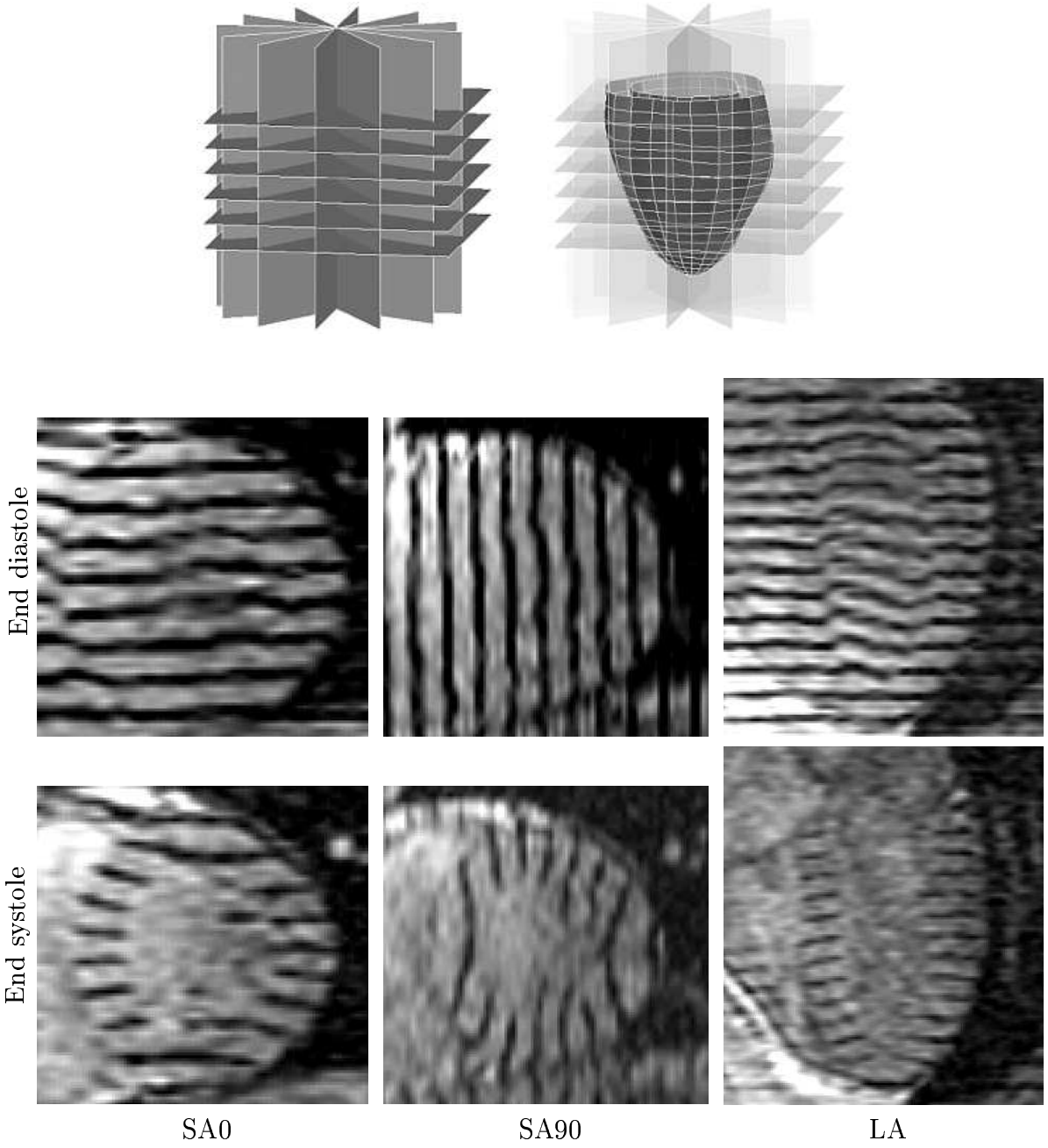


Figure 6: The planar tagged MR images. Top, the region of interest in the short axis and long axis planes. The LV mesh used for the display is showed on the right with the ROI in transparency. Bottom, some images of the LV at end diastole (top) and end systole (bottom) with three different tag directions, from left to right (two short axis and one long axis).

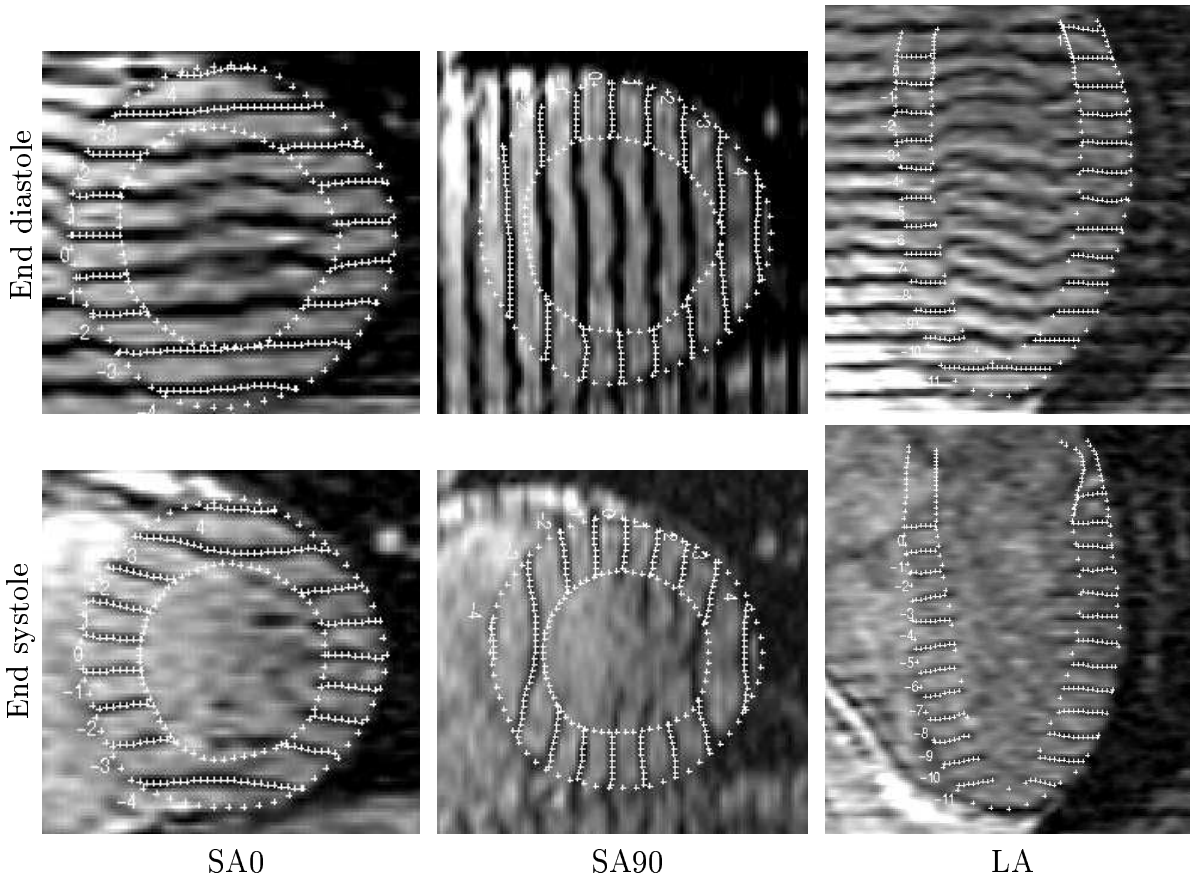


Figure 7: The contours of the LV and the myocardial tags are segmented with the semi-automated package "FindTags" [13] and are represented on top of the images displayed in figure 6.

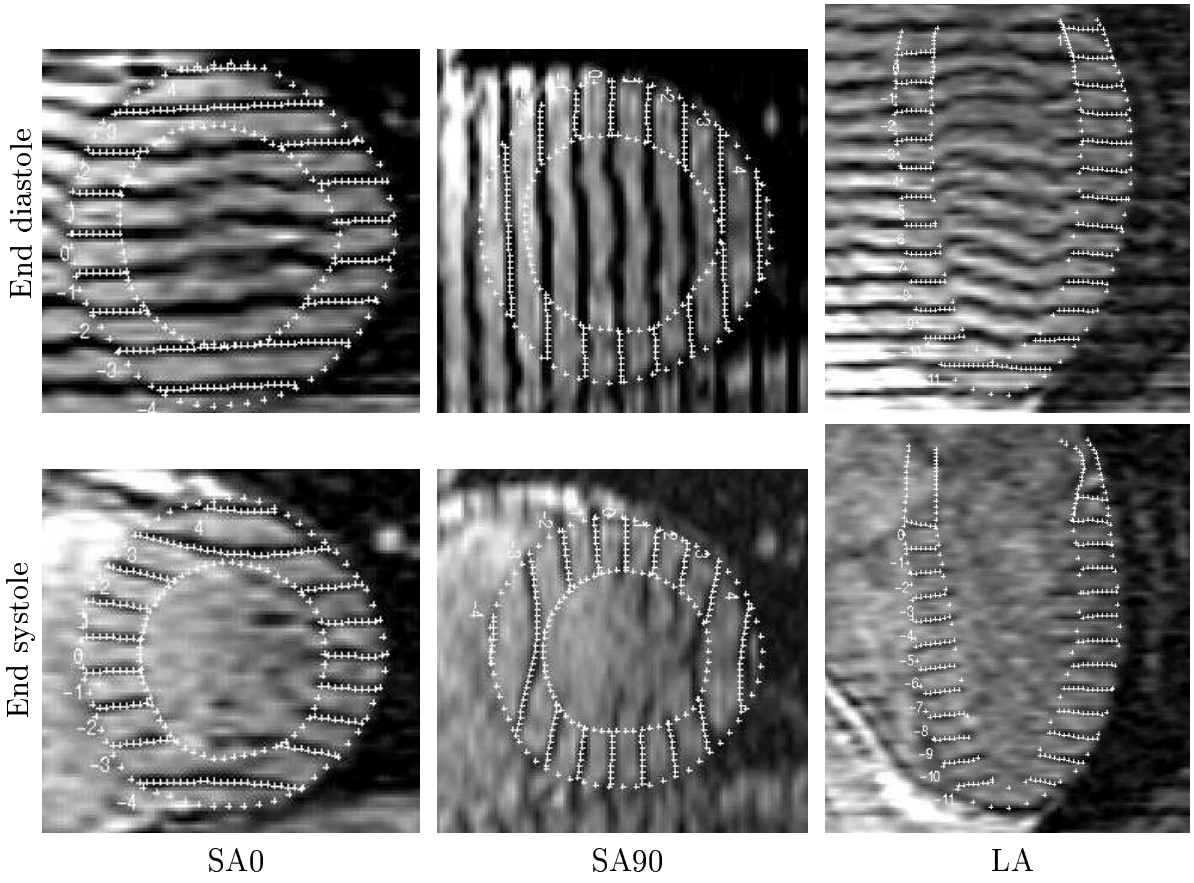


Figure 8: The simulated tags are represented on top of the images of figure 6, their location is to be compared with the tags shown on figure 7.

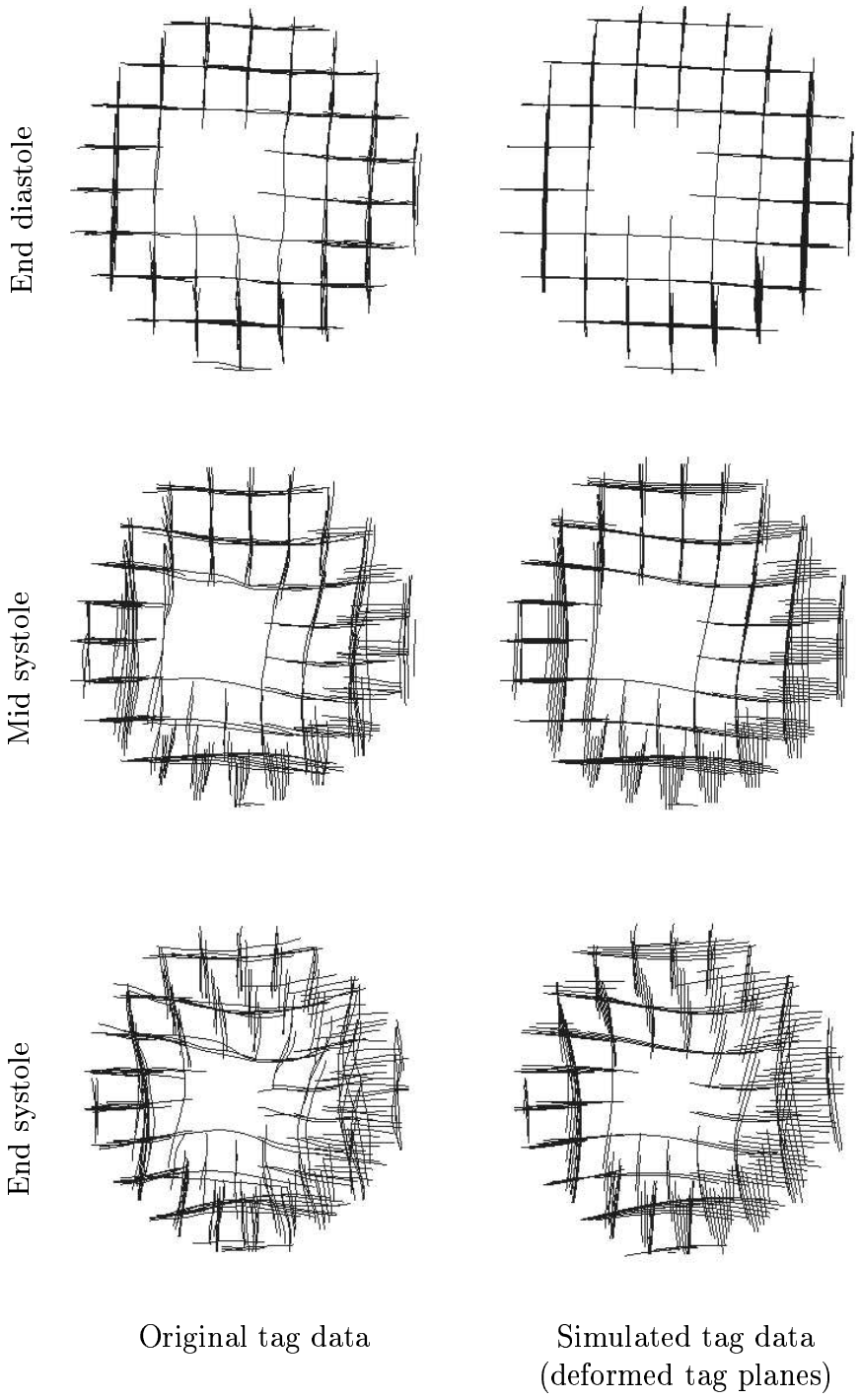


Figure 9: On the left, the short axis tags at three times during systole (the long axis data have been removed for clarity). On the right, the simulated tag data at the same time frames. Each line is the intersection of an image slice and a tag plane deformed by the 4D transformation.

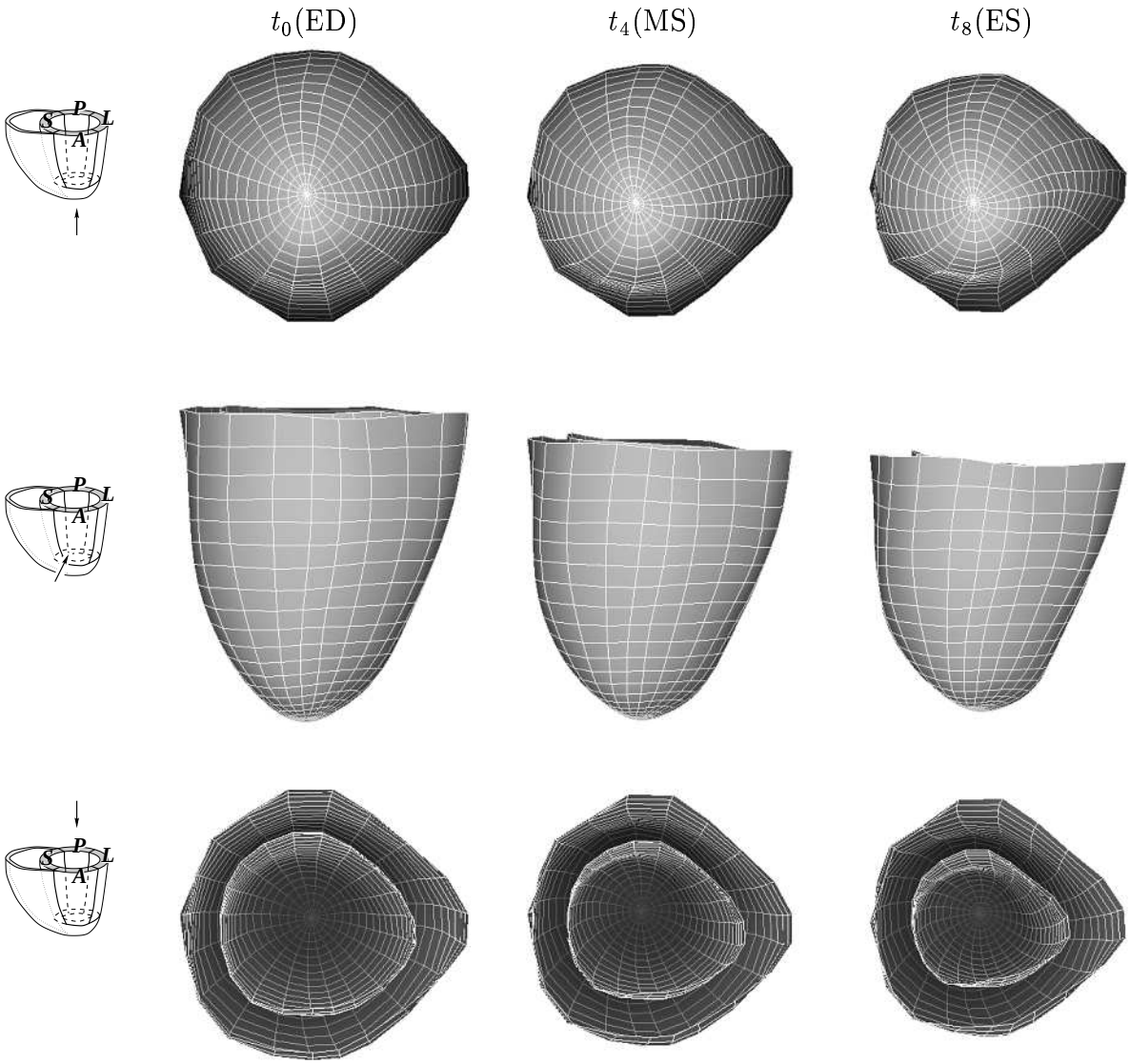


Figure 10: The endocardial and epicardial surfaces of the normal LV is represented with the displayed mesh (septum is on the left). This mesh is deformed with the 4D transformation. From left to right, the shape of the mesh is displayed at 3 times during systole (beginning, mid and end systole). From top to bottom, different views of the surface (apical, anterior and basal views) are displayed for clarity.

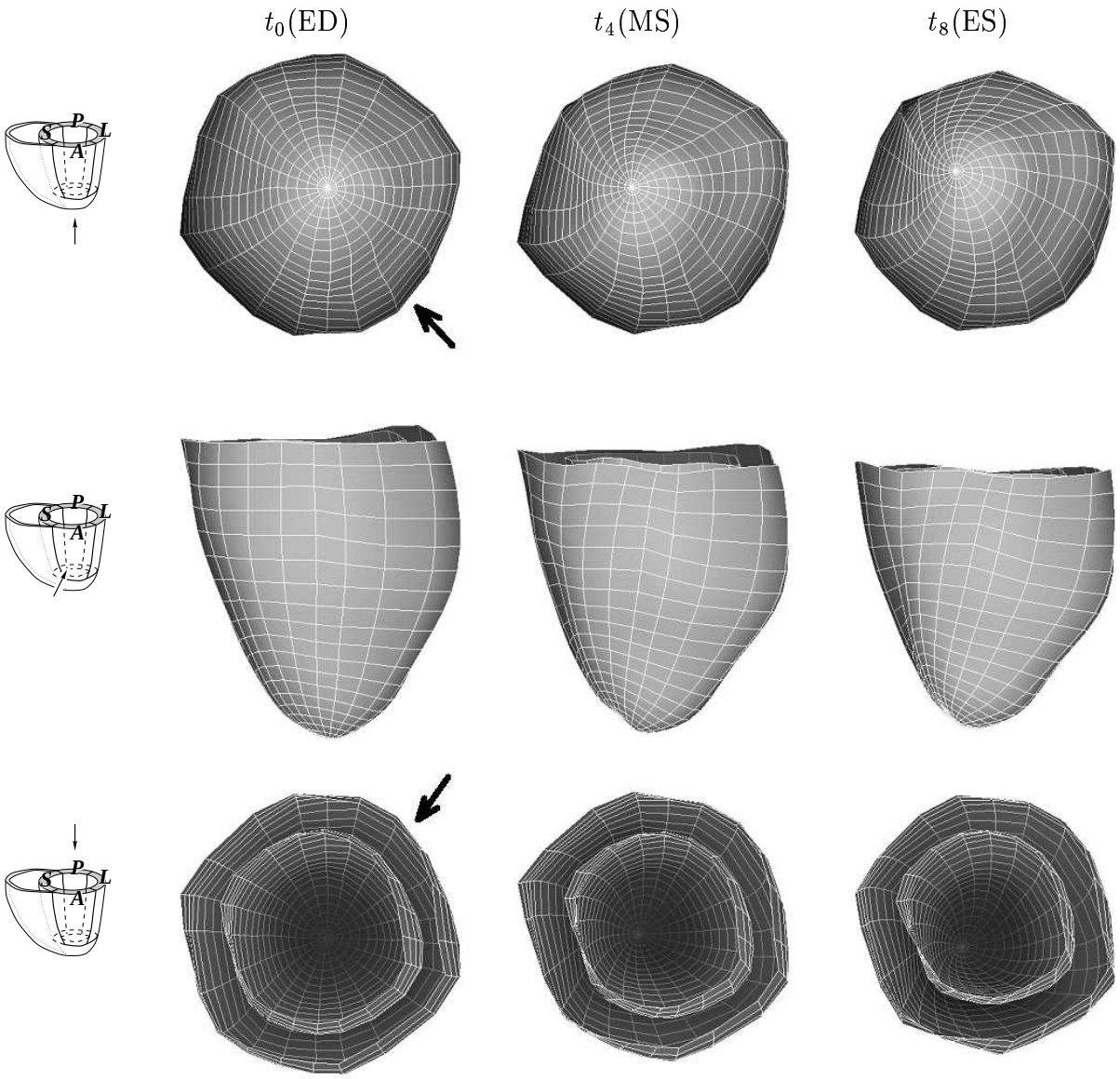


Figure 11: The endocardial and epicardial surfaces of the pathological LV (posterior infarct, pointed by arrow) is represented with the displayed mesh at different times and from different views, as in figure 10.

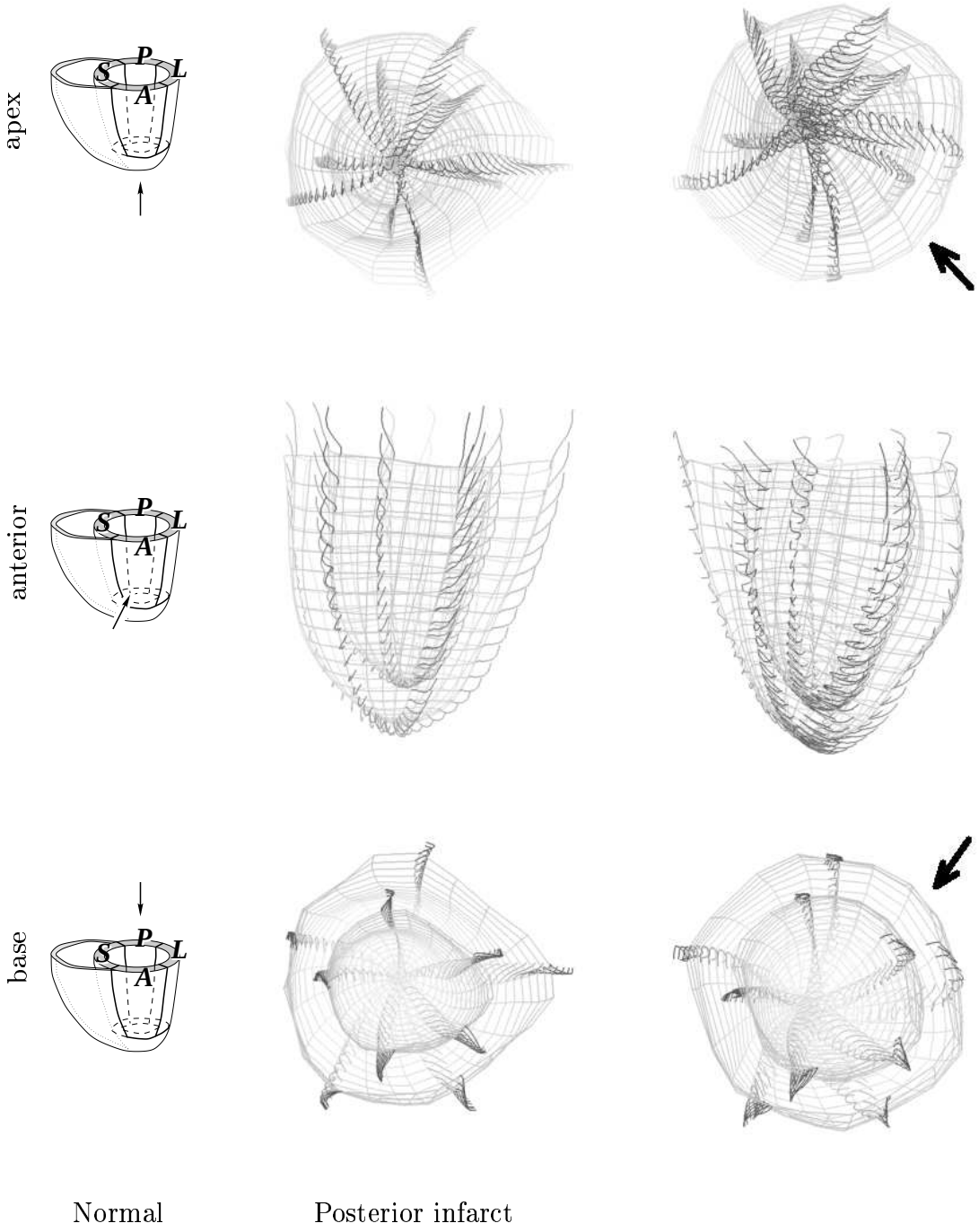


Figure 12: The mesh of the normal LV surfaces is displayed in wireframe at end systole and trajectories of some points over the whole systole are added and shown on three different views. Left, the normal case, right, the pathological case (posterior infarct, pointed by arrow).

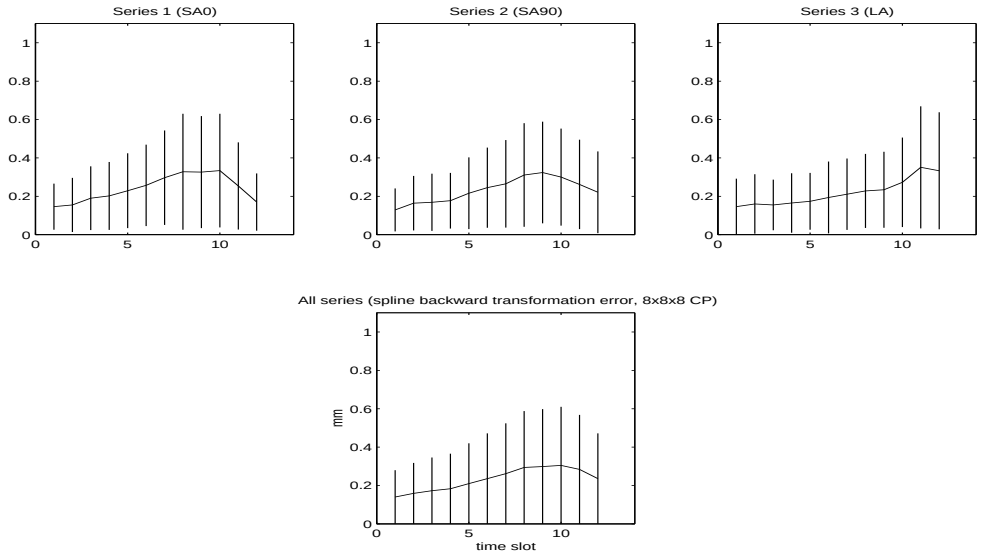


Figure 13: Top, the mean residual distance of the tag points deformed by the backward transformation at each time frame of the sequence, for each of the series (series 1 is SA0, series2 is SA90, series 3 is LA). The vertical lines show the the standard deviation of the error distribution. Bottom, the same graph is displayed for all tag points together.

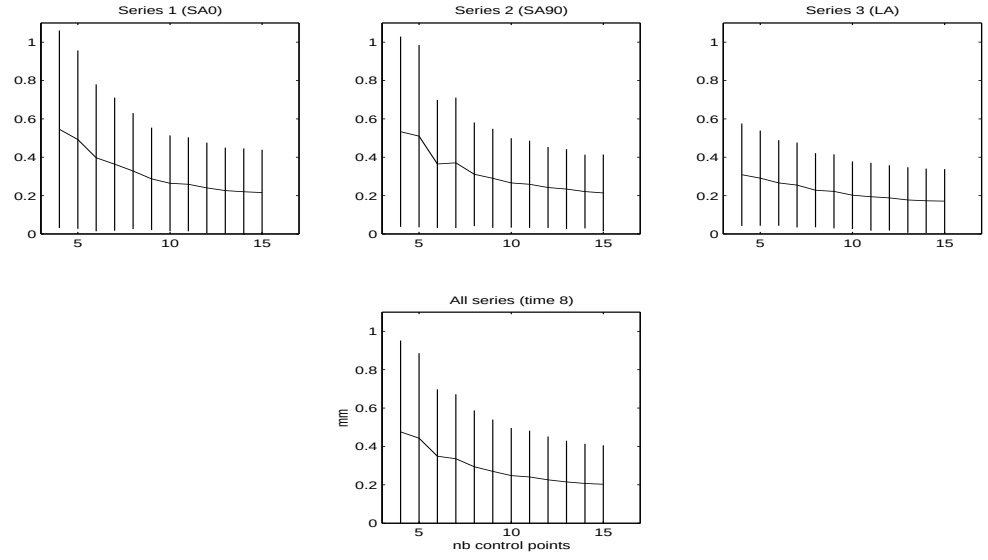


Figure 14: The mean residual distance of the tag points deformed by the backward transformation at end systole for a variable number of control points defining the $\Phi_{n \to T}$, from 4x4x4 to 15x15x15.

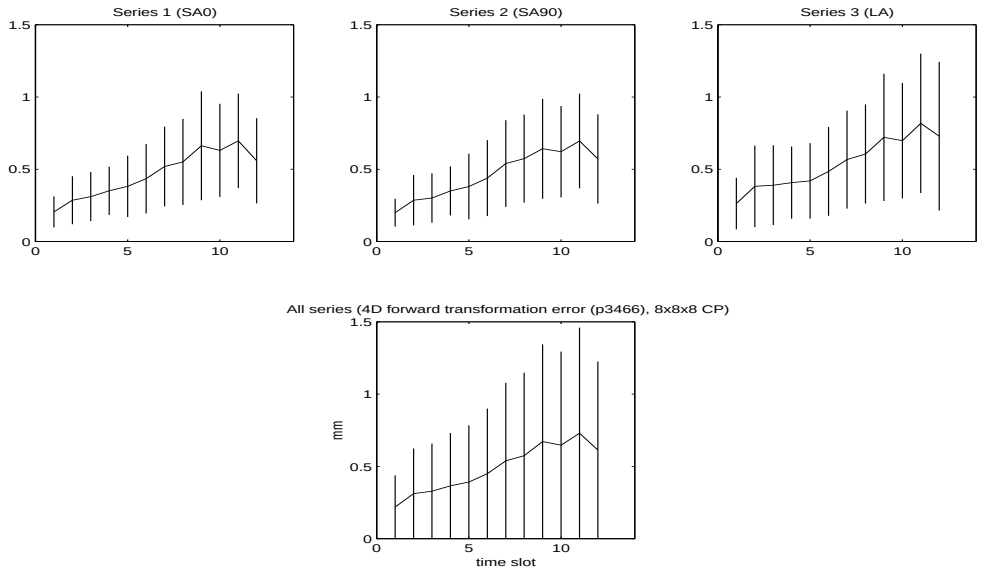


Figure 15: Each tag point is deformed by $\Phi_{n \to T}$ and then deformed by the 4D transformation: the plots represent the mean residual error after this step, for 8x8x8 control points for the backward transformation and 3x3x4x6 for the 4D.

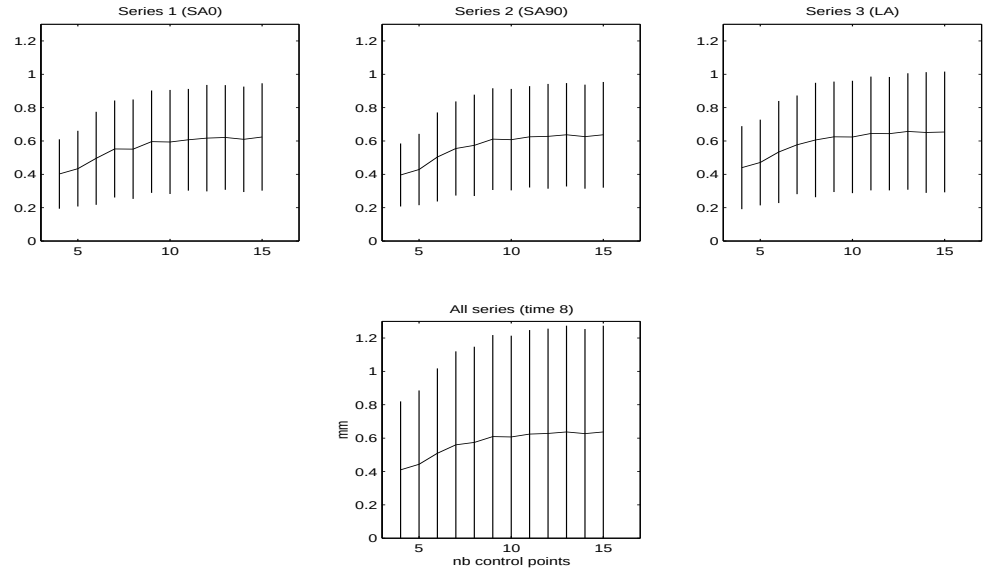


Figure 16: The error graphs as for figure 15, for end systole only and for a variable number of control points, from 4x4x4 to 15x15x15 for the backward transformation.

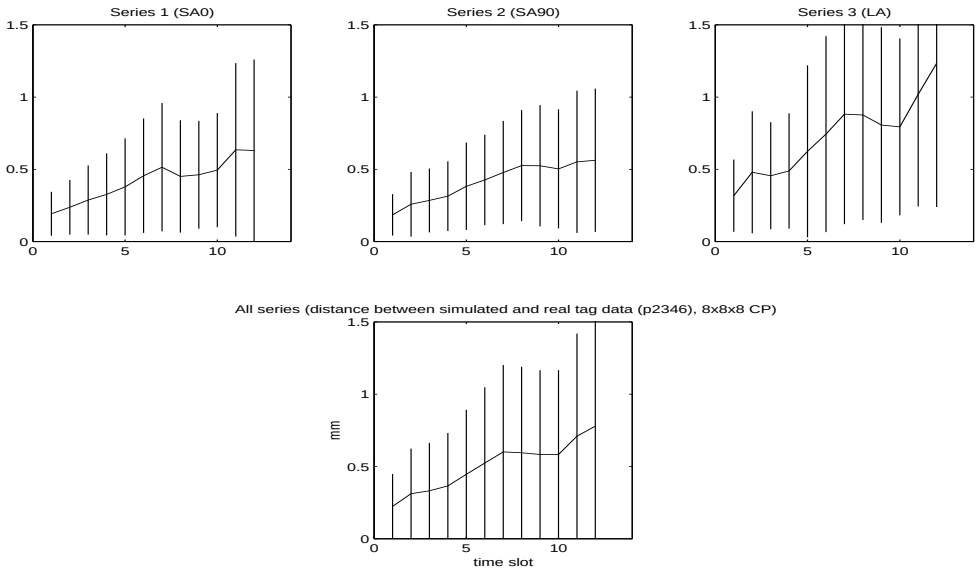


Figure 17: The residual distance between simulated and original tag points, for all time frames. The backward transformation is 8x8x8, the 4D is 2x3x4x6.

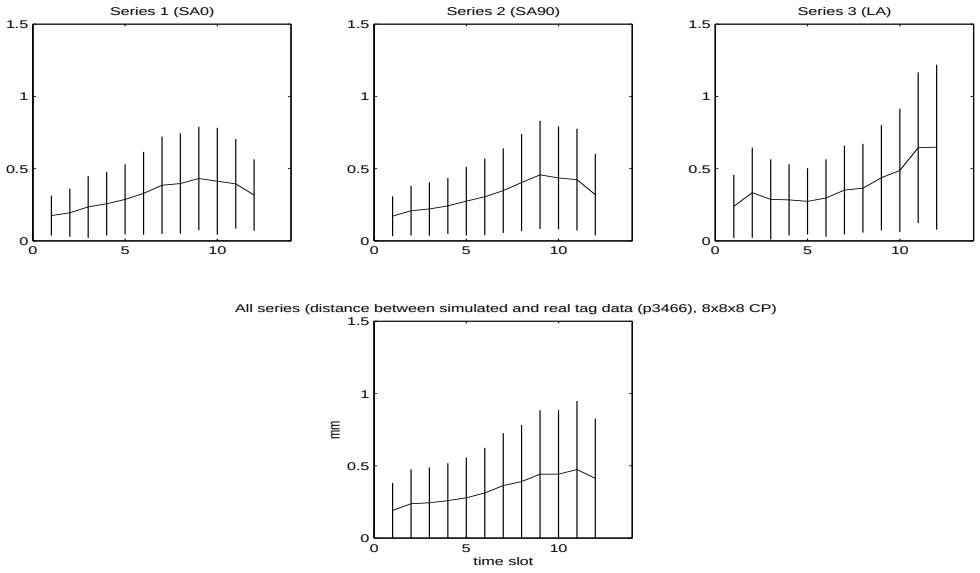


Figure 18: Same as figure 17, for a 4D transformation defined by 3x4x6x6 control points.

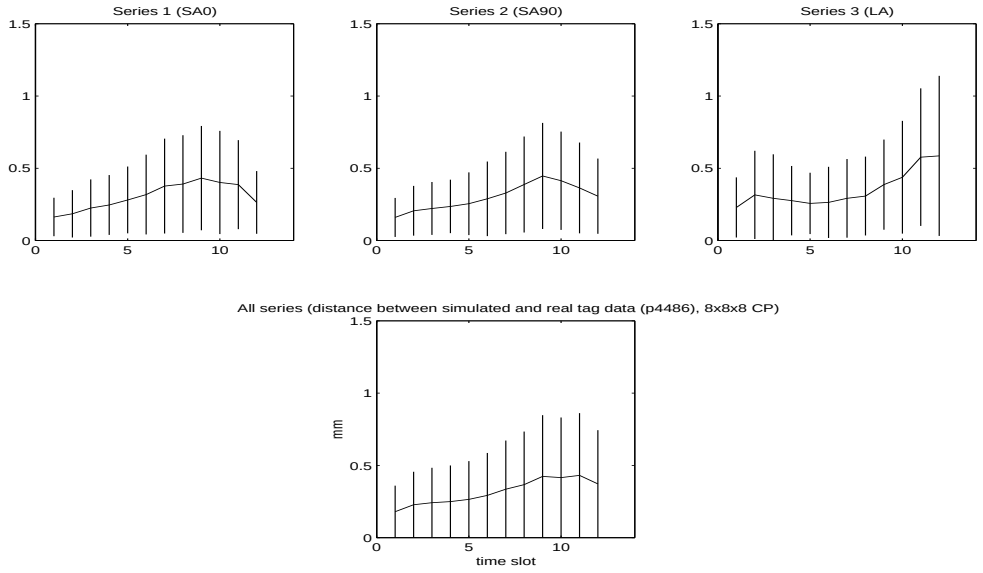


Figure 19: Same as figure 17, for a 4D transformation defined by 4x4x8x6 control points.

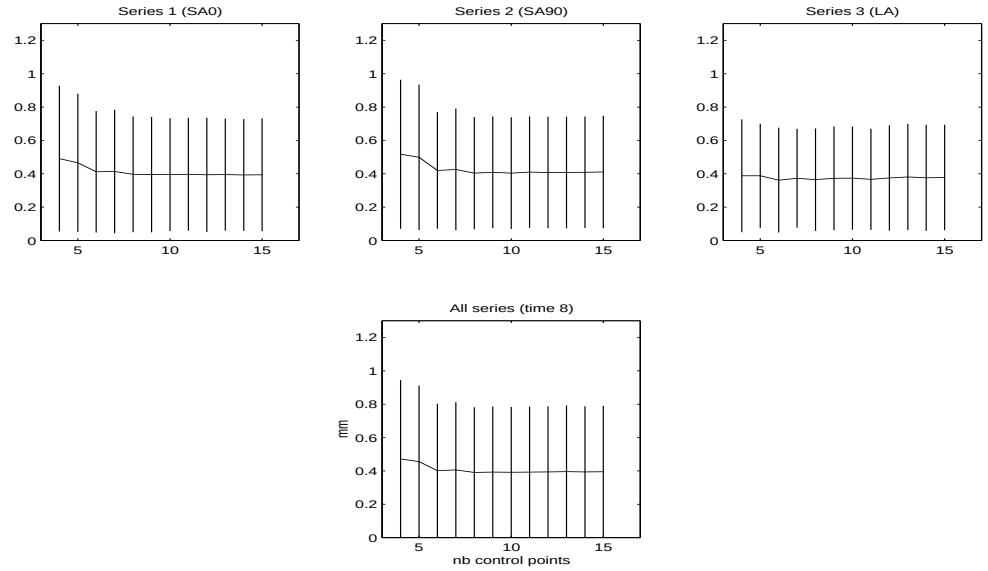


Figure 20: The residual distance between simulated and original tag points at end systole for a variable number of control points for the backward transformation, from 4x4x4 to 15x15x15.

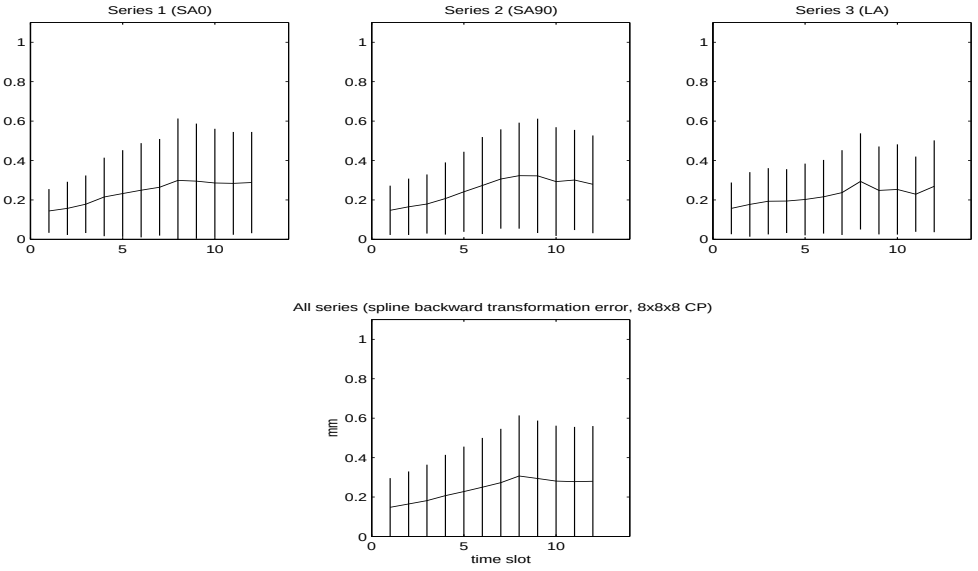


Figure 21: The mean residual distance of the tag points deformed by the backward transformation at each time frame of the sequence of a pathological heart (posterior infarct).

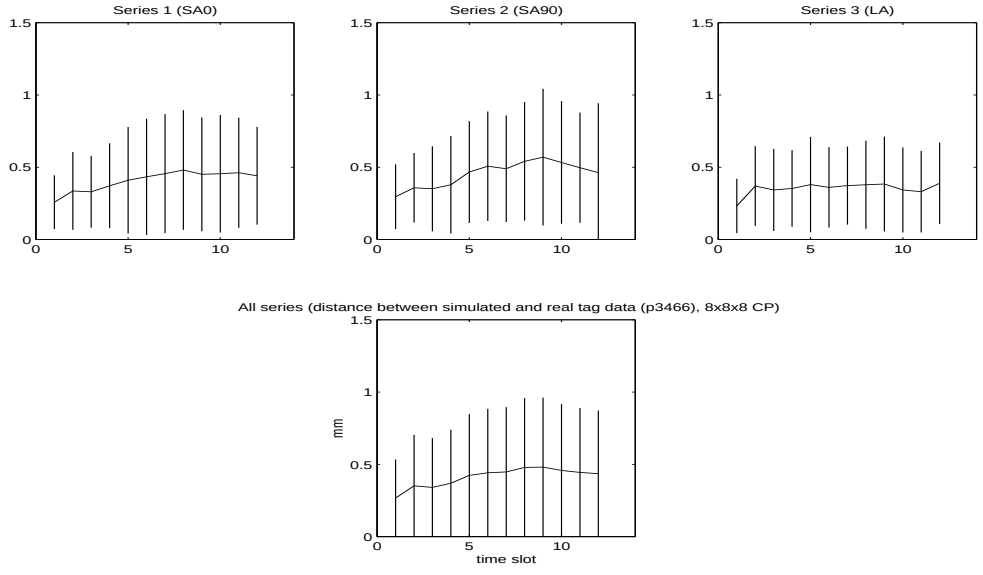


Figure 22: The redisual distance between simulated and original tag points, for all time frames. The transformation backward transformation is 8x8x8, the 4D is 3x4x6x6 for a pathological heart (posterior infarct).

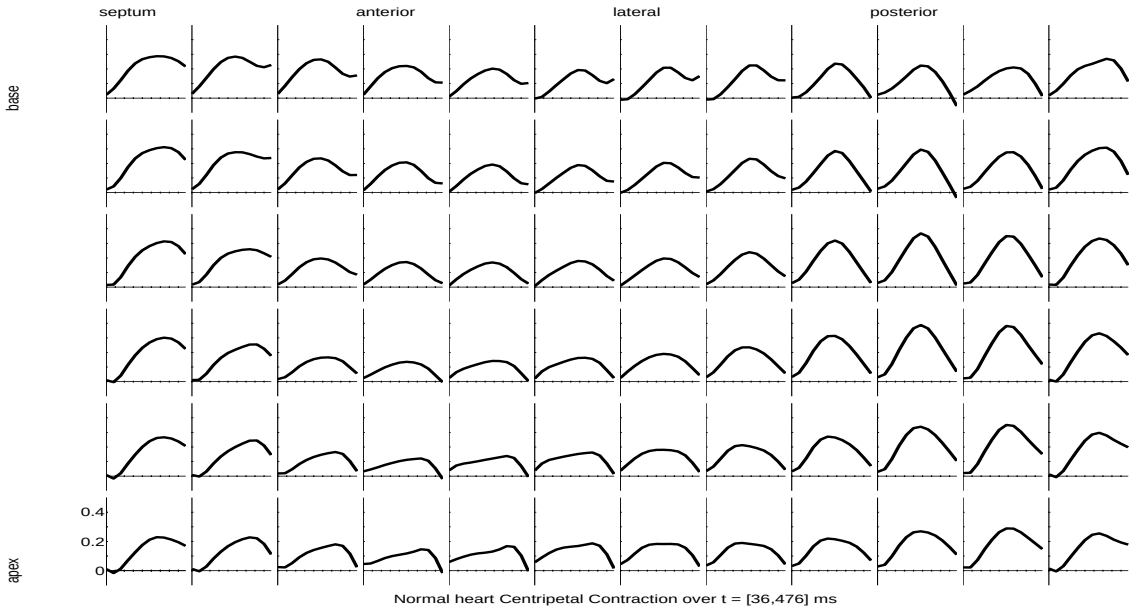


Figure 23: The centripetal contraction (radial motion parameter) derived from the displacement field of a normal LV over systole, from the planispheric 4D transformation.

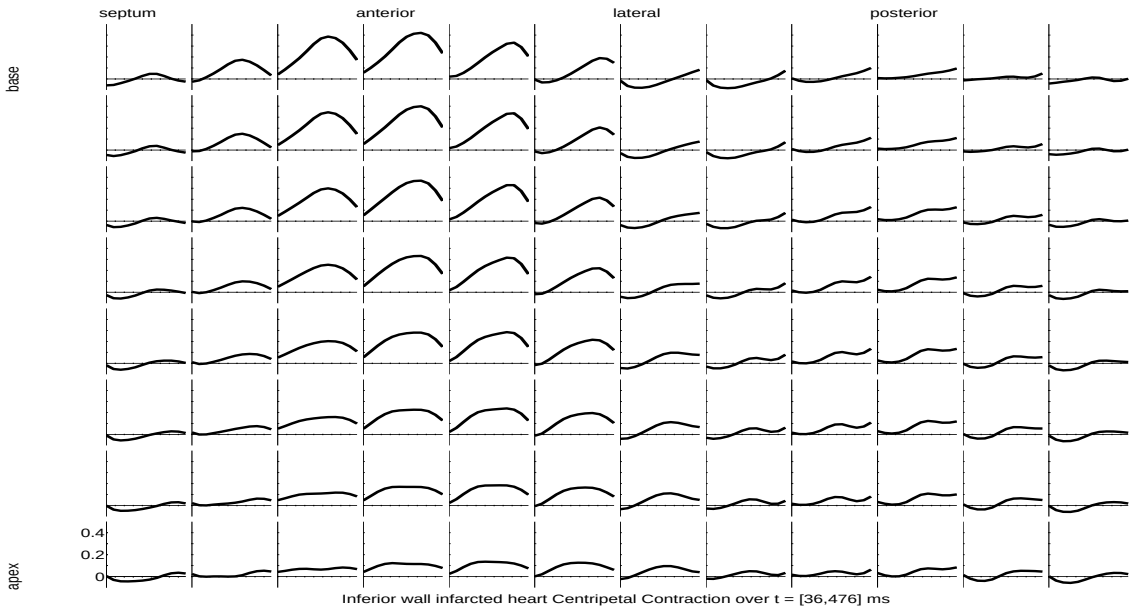


Figure 24: The centripetal contraction (radial motion parameter) derived from the displacement field of a pathological heart (posterior infarct) over systole, as in figure 23.

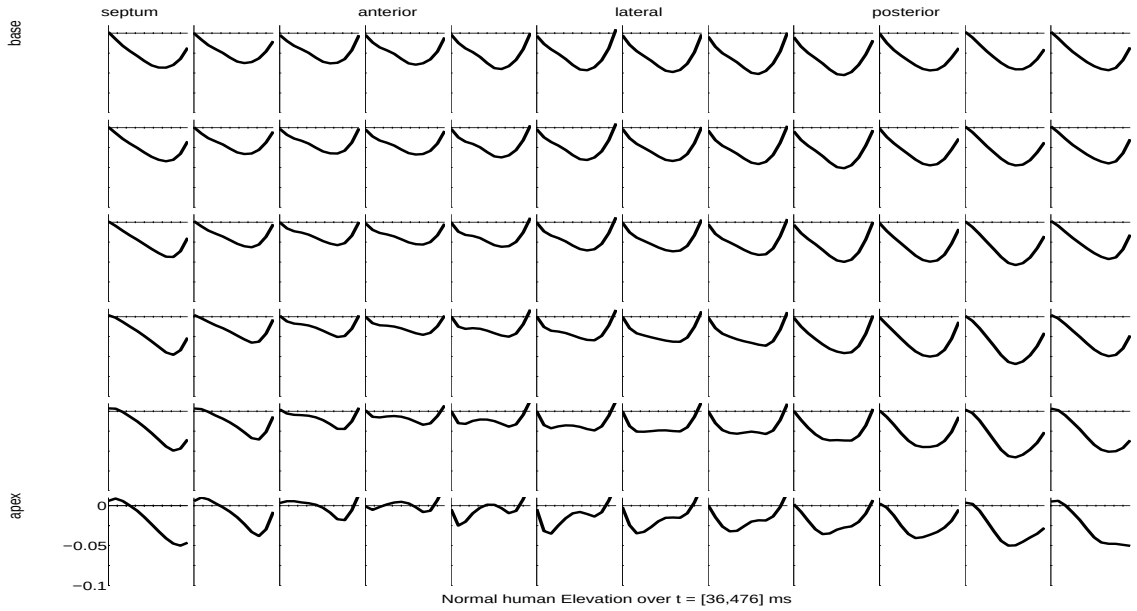


Figure 25: The elevation parameter derived from the displacement field of a normal LV over systole, from the planispheric 4D transformation.

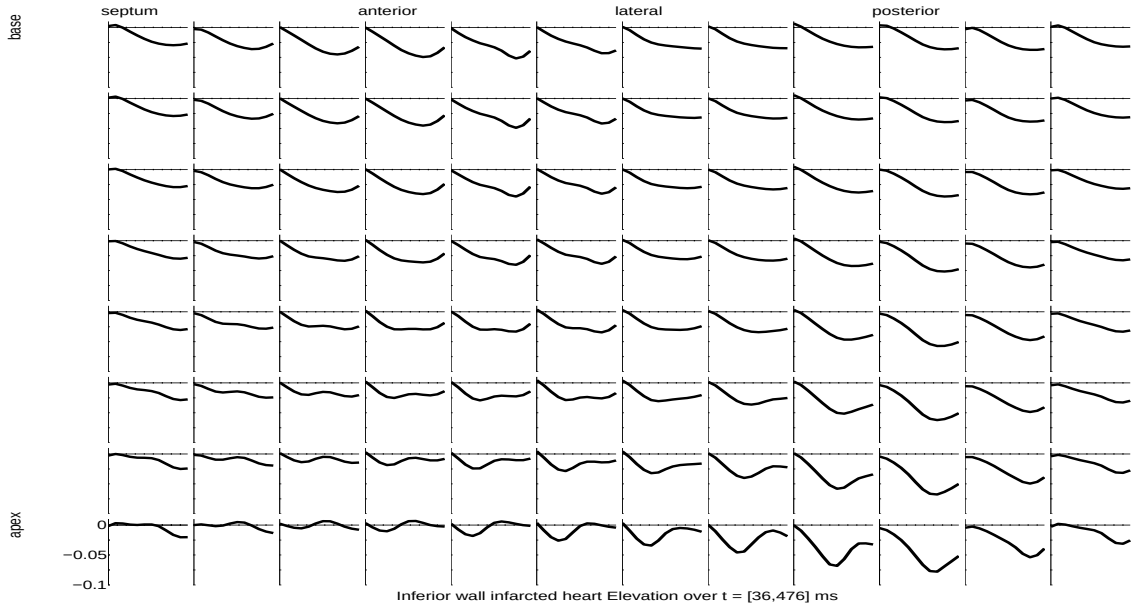


Figure 26: The elevation parameter derived from the displacement field of a pathological heart (posterior infarct) over systole, as in figure 25.

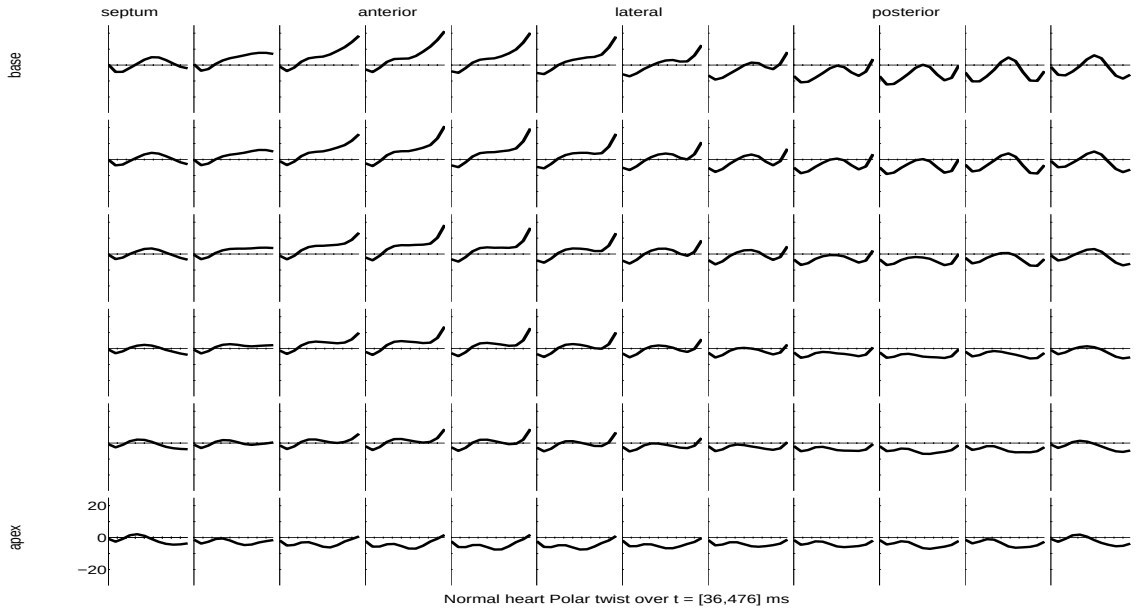


Figure 27: The polar twist (apico-basal rotation parameter) derived from the displacement field of a normal LV over systole, from the planispheric 4D transformation.

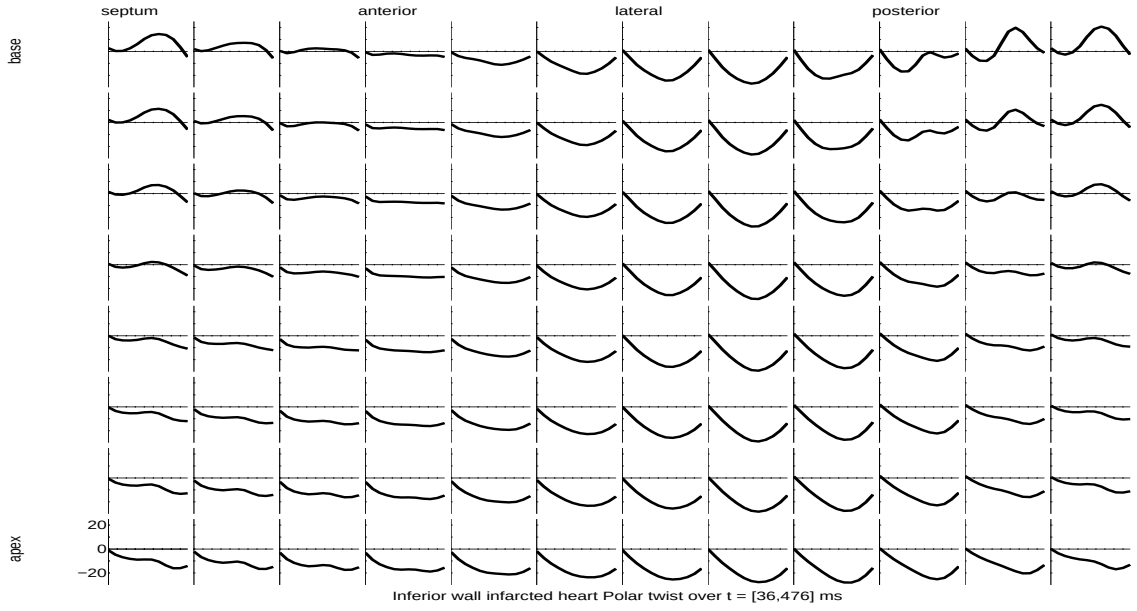


Figure 28: The polar twist (apico-basal rotation parameter) derived from the displacement field of a pathological heart (posterior infarct) over systole, as in figure 27.

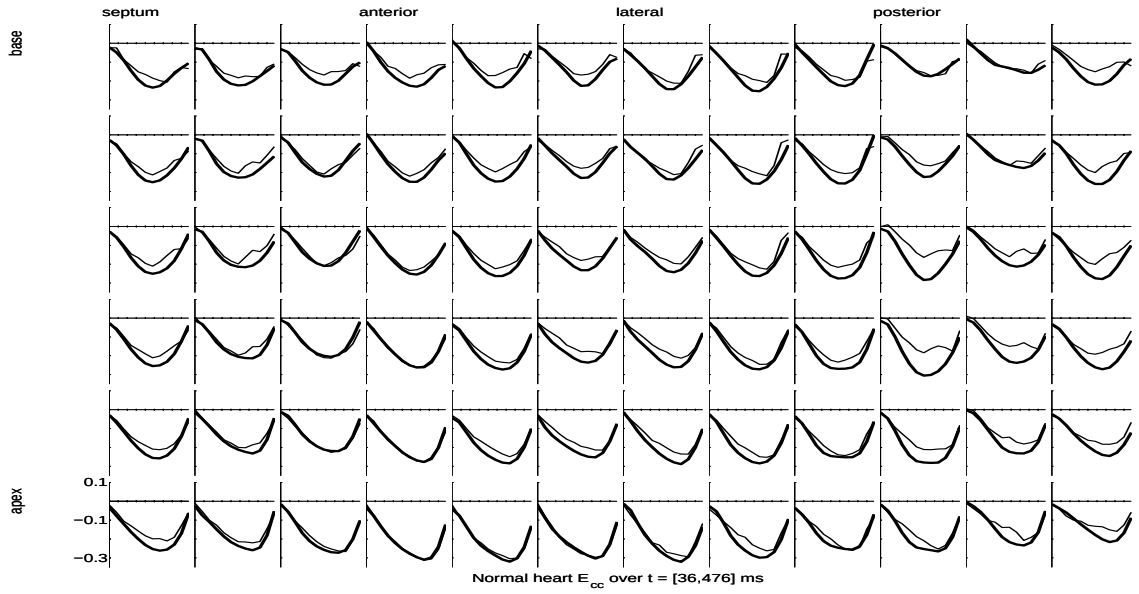


Figure 29: The circumferential strain value E_{cc} derived from the displacement field of a normal LV over systole, from the planispheric 4D transformation (thick lines) and from the "TEA" analysis package [19] (thin lines).

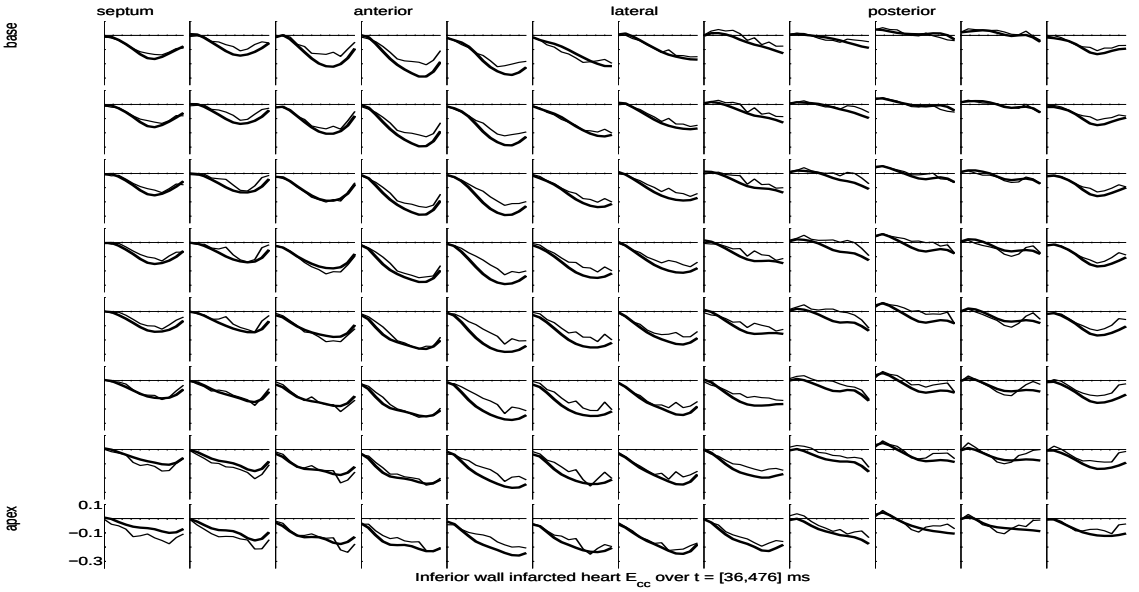


Figure 30: The circumferential strain E_{cc} for a pathological heart (posterior infarct), with two methods as showed in figure 29.

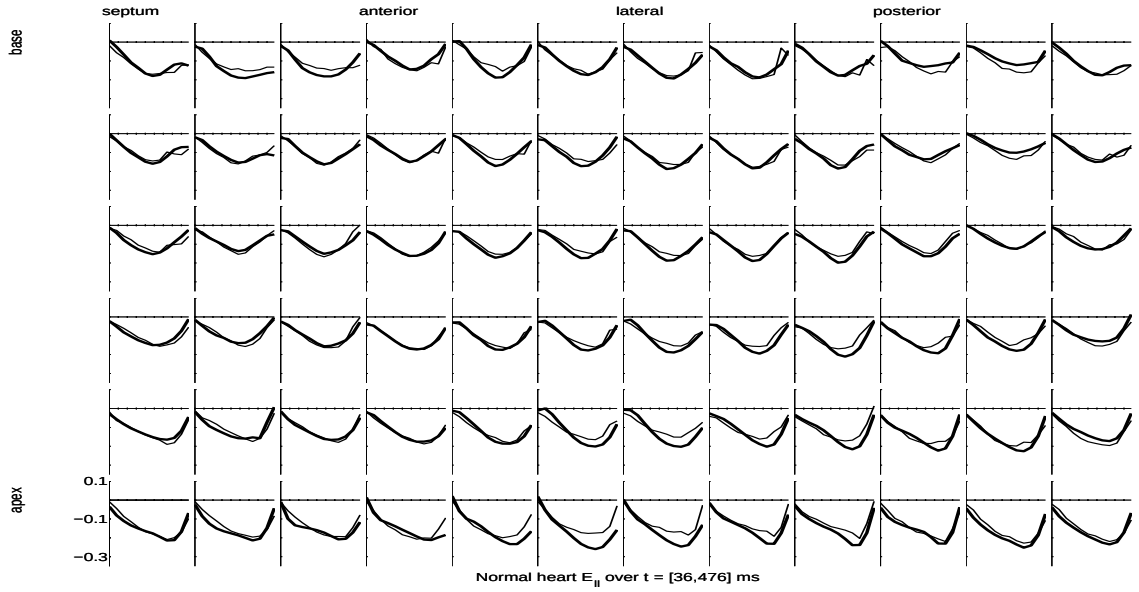


Figure 31: The longitudinal strain value E_{ll} derived from the displacement field of a normal LV over systole, from the planispheric 4D transformation (thick line) and from the "TEA" analysis package [19] (thin lines).

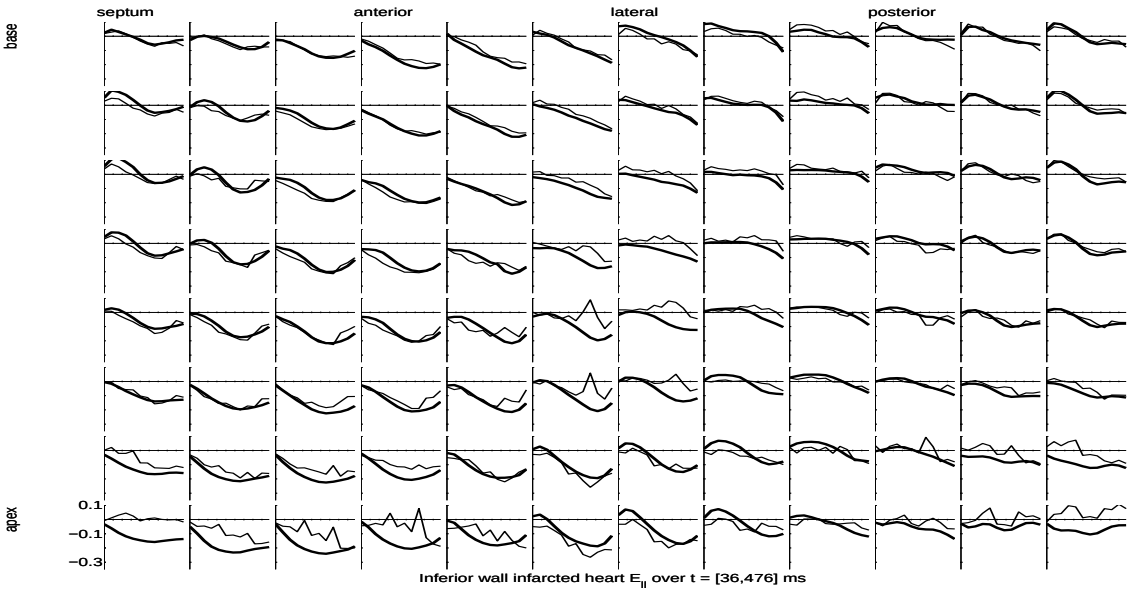


Figure 32: The longitudinal strain E_{ll} for a pathological heart (posterior infarct), with two methods as showed in figure 31.

References

[1] A. Amini, R. Curwen, R.T. Constable, and J.C. Gore. MR Physics-based Snake Tracking and Dense Deformation from Tagged Cardiac Images. In *AIII Spring Symposium Series. Applications of Computer Vision in Medical Image Processing*, March 1994.

[2] T. Arts, W.C. Hunter, A. Douglas, A.M. Muijtjens, and R.S. Reneman. Description of the deformation of the left ventricle by a kinematic model. *Journal of Biomechanics*, 25(10):1119–1127, 1992.

[3] L. Axel and L. Dougherty. MR imaging of motion with spatial modulation of magnetization. *Radiology,*, 171:841–845, 1989.

[4] F.L. Bookstein. Principal warps: thin-plate splines and the decomposition of deformations. *IEEE Transactions on Pattern Analysis and Machine Intelligence*, 11(6):567–585, 1989.

[5] J. Declerck. *Étude de la dynamique cardiaque par analyse d'images tridimensionnelles.* PhD thesis, Université Nice-Sophia Antipolis, November 1997.

[6] J. Declerck, J. Feldmar, and N. Ayache. Definition of a four-dimensional continuous planispheric transformation for the tracking and the analysis of left-ventricle motion. *Medical Image Analysis*, 2(2):197–213, June 1998.

[7] J. Declerck, J. Feldmar, M.L. Goris, and F. Betting. Automatic registration and alignment on a template of cardiac stress & rest reoriented SPECT images. *IEEE Transactions on Medical Imaging*, pages 727–737, December 1997. (Also INRIA Research Report # 2770,http://www.inria.fr/rapports/sophia/RR-2770.html).

[8] J. Declerck, G. Subsol, J.-P. Thirion, and N. Ayache. Automatic retrieval of anatomical structures in 3D medical images. In *Computer Vision, Virtual Reality and Robotics in Medicine*, volume 905 of *Lecture Notes in Computer Science*, pages 153–162. Springer-Verlag, April 1995. (Also INRIA Research Report # 2485).

[9] T. Denney. Identification of myocardial tags in tagged MR images without prior knowledge of myocardial contours. In *Information Processing in Medical Imaging*, volume 1230 of *Lecture Notes in Computer Science*, pages 327–340. Springer-Verlag, June 1997.

[10] T.S. Denney and J.L. Prince. Reconstruction of 3D left ventricular motion from planar tagged cardiac MR images: an estimation theoretic approach. *IEEE Transactions on Medical Imaging*, 14(4):625–635, June 1995.

[11] G. Farin. *Curves and Surfaces for Computer Aided Geometric Design.* Academic Press, Inc., 1989.

[12] M. Guttman, E. Zerhouni, and E. McVeigh. Analysis of cardiac function from MR images. *IEEE Computer Graphics*, pages 30–38, January 1997.

[13] M.A. Guttman, J.L. Prince, and E.R. McVeigh. Tag and contour detection in tagged MR images of the left ventricle. In *IEEE Transactions on Medical Imaging*, volume 13, pages 74–88, March 1994.

[14] P.J. Hunter and B.H. Smaill. The analysis of cardiac function: a continuum approach. *Prog. Biophys. Molec. Biol.*, 52:101–164, 1988.

[15] W. Kerwin and J. Prince. Generating 3-D cardiac material markers using tagged MRI. In *Information Processing in Medical Imaging*, volume 1230 of *Lecture Notes in Computer Science*, pages 313–326. Springer-Verlag, June 1997.

[16] D. Kraitchman, A. Young, C.N. Chang, and L. Axel. Semi-automatic tracking of myocardial motion in MR tagged images. *IEEE Transactions on Medical Imaging*, 14(3):422–433, September 1995.

[17] S. Kumar and D. Goldgof. Automatic Tracking of SPAMM Grid and the Estimation of Deformation Parameters from Cardiac MR Images. In *IEEE Transactions on Medical Imaging*, pages 122–132, March 1994.

[18] M.J. Moulton, L. Creswell, S. Downing, R. Actis, B. Szabo, M. Vannier, and M. Pasque. Spline surface interpolation for calculating 3D ventricular strains from MRI tissue tagging. *American Journal of Physiology*, 270:H281–H297, 1996.

[19] W.G. O'Dell, C. Moore, W.C. Hunter, E.A. Zerhouni, and E. McVeigh. Displacement field fitting for calculating 3D myocardial deformations from tagged MR images. *Radiology*, 195:829–835, 1995.

[20] J. Park, D. Metaxas, and L. Axel. Analysis of left ventricular motion based on volumetric deformable models and MRI-SPAMM. *Medical Image Analysis*, 1(1):53–71, March 1996.

[21] P. Radeva, A. Amini, and J. Huang. Deformable B-Solids and Implicit Snakes for Localization and Tracking of MRI-SPAMM Data. *Computer Vision and Image Understanding*, 66(2):163–178, May 1997.

[22] A. Young, D. Kraitchman, L. Dougherty, and L. Axel. Tracking and Finite Element Analysis of Stripe Deformation in Magnetic Resonance Tagging. *IEEE Transactions on Medical Imaging*, 14(3):413–421, September 1995.

[23] E. Zerhouni, D. Parish, W. Rogers, A. Yang, and E. Shapiro. Human heart: tagging with MR imaging - A method for noninvasive assessment of myocardial motion. *Radiology*, 169(1):59–63, October 1988.



Unité de recherche INRIA Sophia Antipolis
2004, route des Lucioles - B.P. 93 - 06902 Sophia Antipolis Cedex (France)

Unité de recherche INRIA Lorraine : Technopôle de Nancy-Brabois - Campus scientifique
615, rue du Jardin Botanique - B.P. 101 - 54602 Villers lès Nancy Cedex (France)
Unité de recherche INRIA Rennes : IRISA, Campus universitaire de Beaulieu - 35042 Rennes Cedex (France)
Unité de recherche INRIA Rhône-Alpes : 655, avenue de l'Europe - 38330 Montbonnot St Martin (France)
Unité de recherche INRIA Rocquencourt : Domaine de Voluceau - Rocquencourt - B.P. 105 - 78153 Le Chesnay Cedex (France)

Éditeur
INRIA - Domaine de Voluceau - Rocquencourt, B.P. 105 - 78153 Le Chesnay Cedex (France)
http://www.inria.fr
ISSN 0249-6399